RESEARCH ARTICLE | MAY 10 2021

Coupled vibration-dissociation time-histories and rate measurements in shock-heated, nondilute O_2 and O_2–Ar mixtures from 6000 to 14 000 K

Jesse W. Streicher ; Ajay Krish ; Ronald K. Hanson

Physics of Fluids 33, 056107 (2021)
https://doi.org/10.1063/5.0048059

Physics of Fluids ARTICLE scitation.org/journal/phf

Coupled vibration-dissociation time-histories and rate measurements in shock-heated, nondilute O_2 and O_2–Ar mixtures from 6000 to 14 000 K

Cite as: Phys. Fluids 33, 056107 (2021); doi: 10.1063/5.0048059
Submitted: 18 February 2021 · Accepted: 15 April 2021 ·
Published Online: 10 May 2021

View Online Export Citation CrossMark

Jesse W. Streicher,[a] Ajay Krish, and Ronald K. Hanson

AFFILIATIONS

Department of Mechanical Engineering, Stanford University, 440 Escondido Mall, Stanford, California 94305, USA

[a]Author to whom correspondence should be addressed: jessewst@stanford.edu

ABSTRACT

Validation of high-fidelity models for high-temperature hypersonic flows requires high-accuracy kinetics data for oxygen (O_2) reactions, including time-histories and rate parameter measurements. Consequently, shock-tube experiments with ultraviolet (UV) laser absorption were performed to measure quantum-state-specific time-histories and coupled vibration-dissociation (CVDV) rate parameters in shock-heated, nondilute O_2 and oxygen–argon (O_2–Ar) mixtures. Experiments probed mixtures of 20% O_2–Ar, 50% O_2–Ar, and 100% O_2 for initial post-reflected-shock conditions from 6000 to 14 000 K and 26–210 Torr. Two UV lasers—one continuous-wave laser and one pulsed laser—measured absorbance time-histories from the fifth and sixth vibrational levels of the electronic ground state of O_2, respectively. The absorbance time-histories subsequently yielded time-histories for vibrational temperature (T_v) from the absorbance ratio, translational/rotational temperature (T_{tr}) from energy conservation, total O_2 number density (n_{O_2}) from the individual absorbances, and vibrational-state-specific number density ($n_{v''}$) from the Boltzmann population fractions. These state-specific temperature and number density time-histories demonstrate the low uncertainty necessary for high-temperature model validation and provide data to higher temperature than previous experiments. Additional analysis of the temperature and number density time-histories allowed inference of rate parameters in the Marrone and Treanor CVDV model, including vibrational relaxation time ($\tau^{O_2-O_2}$), average vibrational energy loss (ε), vibrational coupling factor (Z), and dissociation rate constants ($k_d^{O_2-O_2}$ and $k_d^{O_2-O}$). The results for each of these five parameters show reasonable consistency across the range of temperatures, pressures, and mixtures and generally agree with a modified Marrone and Treanor model by Chaudhry *et al.* ["Implementation of a chemical kinetics model for hypersonic flows in air for high-performance CFD," in Proceedings of AIAA Scitech Forum (2020)]. Finally, the results for $\tau^{O_2-O_2}$, $k_d^{O_2-O_2}$, and $k_d^{O_2-O}$ exhibit much lower scatter than previous experimental studies.

I. INTRODUCTION

Chemical and vibrational nonequilibrium in high-temperature, shock-heated oxygen (O_2) strongly influences the thermodynamic state of air in the flow fields around hypersonic and reentry vehicles.[2–4] Generally, nonequilibrium in high-temperature air includes internal energy excitation, chemical reactions, ionization, and radiative emission, with all of these processes influencing vehicle heating.[5–7] Of these processes, internal energy excitation (rotational, vibrational, and electronic excitation) and chemical reactions (dissociation, recombination, and exchange reactions) involve smaller energy changes than ionization or radiative emission, and thus they strongly influence high-temperature air over a wide range of temperatures and flight speeds.

O_2 nonequilibrium especially impacts the thermodynamic state of high-temperature air because O_2 dissociates at lower temperatures than nitrogen (N_2), and the resulting O atoms subsequently break N_2 bonds through the Zeldovich reactions.[8–10] Additionally, O_2 has smaller spacing between adjacent vibrational energy levels than N_2, resulting in faster vibrational excitation.[11–13] However, the O_2–N_2 interactions in shock-heated air involve many possible collision partners and reaction outcomes, so experiments benefit from restricting the investigation to focus on a subset of these reactions. While air contains only about 1% argon (Ar), O_2–Ar mixtures were used in this work to simplify the reaction set and to access high temperatures. Higher O_2 concentrations in this work allowed the study of vibrational excitation and dissociation via O_2–O_2 and O_2–O collisions. A previous study, using similar methods to the current work, studied vibrational excitation and dissociation via O_2–Ar collisions in highly dilute mixtures; those results are leveraged in this work.[14] However, the inclusion

of Ar in the current experiments provided the additional benefit of accessing high temperatures with lower Mach number shocks. The use of higher O_2 concentration mixtures, together with previous O_2–Ar studies, provided the means to study nonequilibrium in O_2–O_2 and O_2–O collisions—an important subset of the collisions that influence high-temperature air—at higher temperatures than any known previous experiments.

For the current work, O_2 was probed behind reflected shocks in a shock tube using two ultraviolet (UV) laser systems, and the UV laser systems each probed a specific vibrational level of the electronic ground state of O_2.[14–20] O_2 was selected as a target species due to strong absorbance features accessible with modern UV laser systems.[15,16,19–24] These features arise from the Schumann–Runge bands, which were initially studied to investigate atmospheric photochemistry, but recent work has used these absorption features to study high-temperature O_2 nonequilibrium.[14,17,18,25] Compared to previous studies that relied on interferometry, emission, or UV absorption from broadband lamp sources, the current laser absorption diagnostics provide a much more sensitive probe of O_2 quantum states.[25–28] Together, the two *in situ* UV laser absorption diagnostics provide a sensitive, quantum-state-specific probe of vibrational temperature and state-specific number density in nonequilibrium O_2.

At the typical temperatures of high-enthalpy hypersonic flow fields, vibrational energy transfer significantly impacts the chemical kinetics (and vice versa) in a process called coupled vibration-dissociation (CVDV).[29,30] As CVDV processes strongly impact the thermodynamic state of O_2 in high-temperature air, many computational models have been developed to simulate this behavior, but the lack of low-uncertainty experimental data has limited model validation.[1,25,29–34] To aid model validation, the current study applies modern UV laser diagnostics to shock-tube experiments to investigate CVDV processes in nondilute O_2 and O_2–Ar mixtures. The shock tube produces repeatable and controlled temperature and pressure conditions relevant to hypersonic flight in air, thus reflecting relevant test cases for model validation. Concomitantly, the UV lasers provide a fast, *in situ*, and quantum-state-specific method to probe vibrational temperature and vibrational state populations, thereby probing quantities of interest for CVDV model validation. The vibrational-state-specific time-histories and CVDV rate parameters results from current experiments demonstrate sufficient sensitivity for high-fidelity model validation of high-temperature O_2 in hypersonic flows.

II. METHODS

Sections II A–II C describe the setup of the shock tube and laser absorption diagnostics, the framework of the CVDV model used for data interpretation, and the analysis procedure to reduce the raw data to quantum-state-specific time-histories and CVDV rate parameters. Many aspects of the experimental setup, CVDV models, and data analysis were previously described for highly dilute O_2–Ar mixtures in Ref. 14. While some relevant details are repeated, this section emphasizes the inclusion of a new UV laser diagnostic and the changes to the procedure for mixtures with a higher O_2 concentration.

A. Experimental setup

The experimental setup for this work consisted of a pressure-driven shock tube augmented with two UV laser diagnostics (Fig. 1). The shock tube was used to generate composition, temperature, and pressure conditions relevant to hypersonic flight behind the reflected shock.[35] Two UV laser diagnostics—one continuous-wave (CW) laser and one picosecond-pulsed laser—observed the transient, nonequilibrium behavior of O_2 in the high-temperature test gas by probing the fifth and sixth vibrational levels of the ground electronic state of O_2.[19–23] While the shock tube and picosecond-pulsed UV laser were used previously to study highly dilute O_2–Ar mixtures, the addition of the CW laser in this work resulted in a vibrational temperature diagnostic that was less sensitive to translational/rotational temperature and eliminated the need to repeat shock experiments by measuring two wavelengths simultaneously.[14,20]

1. Shock-tube setup

The shock tube used to generate the 6000–14 000 K and 26–210 Torr conditions was pressure-driven with a stainless steel, 15.24 cm diameter, electropolished interior (Fig. 1).[14–20] The shock waves were formed by bursting polycarbonate diaphragms ranging in thickness from 0.18 to 0.51 mm that separated the low-pressure test mixtures from the high-pressure helium driver gas. Changing the diaphragm thickness and test gas fill pressure provided control of the incident shock velocity, thereby achieving the desired initial post-reflected-shock temperature and pressure.[36] The fill pressure was measured with a 0–100 Torr capacitance manometer (Baratron, MKS Instruments), and the diaphragm burst pressure was measured with a 0–3000 psia capacitance manometer (280E, Setra Systems). Additionally, five piezoelectric pressure transducers (483A11, PCB Piezotronics, Inc.) were used to measure the shock velocity and shock attenuation. Finally, pressure at the laser observation location—5 mm from the end wall—was measured with a low-noise piezoelectric pressure transducer (5010B, Kistler Instrument Corp.), thus tracking the slight, non-ideal pressure rise. A full summary of the initial post-reflected-shock temperature and pressure, non-ideal pressure rise, fill pressure, shock velocity, and shock attenuation for each experiment can be found in Tables II–IV in Appendix B.

The composition of the test gas was largely determined by the mixture preparation, but leak rates were also monitored to ensure ambient air did not influence the mixture composition. The 20% and 50% O_2–Ar mixtures were prepared manometrically in a mixing tank from pure gases, while the 100% O_2 gas was filled directly from the pure compressed gas cylinder (Praxair Technology, Inc.). Prior to each experiment, ambient air was evacuated from both the driver and driven sections using rotary pumps (Varian 949, Agilent, Inc.), but the driven section was further evacuated using a turbomolecular pump (Varian 969, Agilent, Inc.). The ultimate pressures achieved with the turbomolecular pump were less than 1.7×10^{-5} Torr as measured by a hot-filament ionization gauge (I-075-K, Duniway Corp.). This ionization gauge was also used to measure the leak rate before each experiment, and these measured leak rates were typically less than 2×10^{-4} Torr/min. Experiments were timed to ensure no more than two minutes passed between isolating the shock tube and the start of a shock experiment, thereby ensuring that the pressure change due to leaks remained below 4×10^{-4} Torr. Since the lowest fill pressure was 0.04 Torr, pressure change due to leaks contributed less than 1% to composition uncertainty. This combination of manometric mixture preparation and careful monitoring of leak rates provided precise control of the test gas composition.

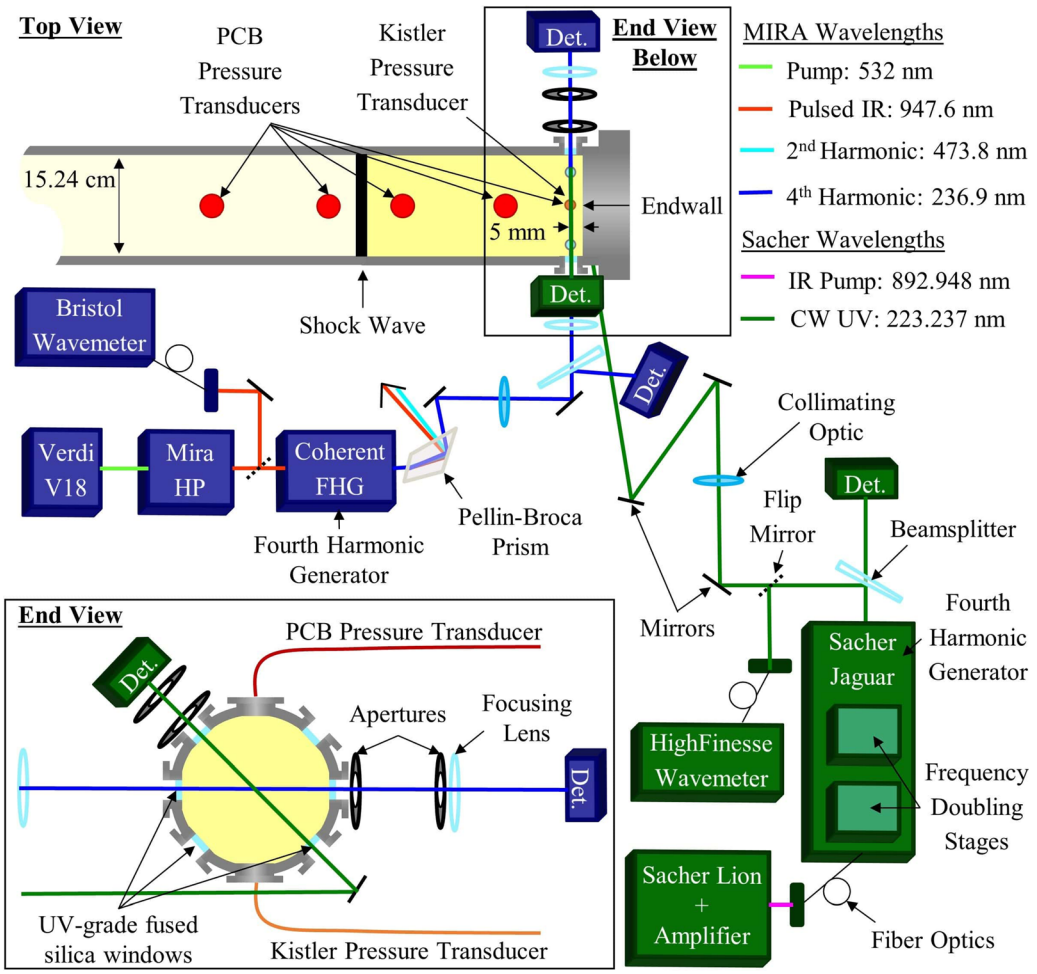

FIG. 1. Arrangement of the shock tube and two UV laser diagnostics used to study coupled vibration-dissociation in nondilute O_2 and O_2–Ar mixtures. Components of the pulsed UV laser system are shown in blue, whereas components of the CW UV laser system are shown in green. Both a top view and end view are provided to clarify the laser alignment through the shock tube.

2. UV laser diagnostics

The two UV laser diagnostics used to probe O_2 in the Schumann–Runge bands consisted of a continuous-wave (CW) UV laser system (Sacher Lasertechnik GmbH) and a picosecond-pulsed UV laser system (Coherent, Inc.) (Fig. 1). The multiple modules of each system were used to generate pump light at the desired wavelength, to manipulate the frequency to produce UV light, and to monitor the laser output wavelength. Once the UV laser light was produced, both systems used the same optical strategies to mitigate laser intensity noise, density steering, and test gas emission.

a. Continuous-wave UV laser diagnostic. The CW laser system was composed of two integrated modules: one to produce and amplify the near-infrared (NIR) pump light and one to quadruple the laser frequency, thereby producing the desired UV light (Fig. 1). The initial NIR pump light was produced using a Littman/Metcalf external cavity diode laser (Lion, Sacher Lasertechnik) with a linewidth less than 100 kHz. This NIR pump light was additionally amplified within the first module using a tapered semiconductor optical amplifier (Serval, Sacher Lasertechnik). The fourth harmonic generation was achieved by routing the pump light using fiber optics into the second module containing two cascaded resonant cavities, each with frequency doubling crystals (Jaguar, Sacher Lasertechnik). Finally, a UV wavemeter (WS/6–200 UVII, HighFinesse GmbH) was used to monitor the center wavelength prior to each experiment. For this work, the pump laser was tuned to 892.948 nm to produce CW UV light at 223.237 nm, which probed the fifth vibrational level of O_2 ($v'' = 5$). The development and validation of a spectroscopic model for this laser and wavelength were recently completed using dilute O_2–Ar mixtures.[20]

The addition of a continuous-wave UV laser system to the experimental setup of this study improved the ability to probe nonequilibrium O_2 compared to previous studies.[14,18] In particular, the monochromatic light produced by this laser system improved the sensitivity of the diagnostic by reducing the number of probed spectral lines. Additionally, the simultaneous use of two UV laser systems

eliminated the need to repeat shock experiments, thereby reducing the uncertainty associated with slightly mismatched post-reflected-shock conditions.[14] Overall, this CW laser diagnostic significantly improved the ability to measure vibrational temperature and state-specific number density.[20]

b. Pulsed UV laser diagnostic. The picosecond-pulsed UV laser system was composed of three integrated modules and produced UV light via two steps of frequency manipulation as described previously.[14–19] First, a continuous-wave, 532 nm Nd:YAG laser (Verdi V18, Coherent, Inc.) pumped a Ti:Sapphire laser system (Mira HP, Coherent, Inc.) to produce pulsed, near-infrared (NIR) light at 947.6 nm (Fig. 1).[37] The NIR laser system was able to produce wavelengths from 700 to 1000 nm, but the current work used 947.6 nm consistently. This pulsed NIR light was then frequency quadrupled (Fourth Harmonic Generator, Coherent, Inc.) resulting in the desired pulsed UV light at 236.9 nm, which probed the sixth vibrational level of O_2 ($v'' = 6$).[19] Finally, the pulsed UV light was separated from the other wavelengths using a Pellin–Broca prism.

The pulses exhibited a repetition rate of 76 MHz and a pulse width of less than 2 ps, effectively providing a continuous wave (CW) recording on the detection system. Though the data acquisition system sampled at 100 MHz, the detection optics were limited by the 900 kHz bandwidth of the silicon optical detectors. As such, the 76 MHz repetition rate pulses were not individually resolved, and the detectors captured the 30 mW of average power from the UV pulses instead.[18] However, the pulsed nature of the NIR and UV light resulted in a laser output with non-negligible spectral width. The NIR output of the Ti:Sapphire laser system produced a Gaussian spectral profile with a full width at half maximum (FWHM) of 0.45 nm as measured by a spectrum analyzer (721, Bristol Instruments). This Bristol spectrum analyzer also monitored the laser center wavelength for the NIR output, though a UV wavemeter was used to confirm the center wavelength of the UV output (WS/6–200 UVII, HighFinesse GmbH). Ultimately, the fundamental wavelength output and FWHM of the Ti:Sapphire laser were recorded both before and after each experiment to account for slight drifts and to ensure that the absorbance model accurately captured the operating condition of the laser for each experiment.[19]

c. Optical strategies. To ensure sensitive absorbance measurements for each of the two UV laser absorption diagnostics, apertures were positioned along the beam paths to prevent test gas emission from reaching the detectors, lenses focused the beams at the center of the shock tube, and two detectors were used in each optical train to account for intensity fluctuations (Fig. 1). The beam paths were located 5 mm from the end wall and had an absorbing path length of 15.24 cm (the internal diameter of the shock tube) resulting in strong absorbance signals. This setup used a pair of large-collection-area silicon optical detectors (New Focus 2032, Newport Corp.) for each beam path to reject laser intensity fluctuations, a strategy referred to as common mode rejection. Also, each of the four detectors was operated in the low-gain setting to provide access to the highest, 900 kHz, bandwidth. The 5.8 mm diameter detection area of the optical detectors, together with focusing lenses, largely negated any effects of density steering on the signal quality of the transmitted beams. Finally, two apertures were co-aligned with each of the two laser beams to prevent emission from the hot test gas from reaching the detector. Overall, these optical strategies ensured high-quality absorbance measurements and rendered competing effects negligible.

B. Coupled vibration-dissociation model

Modeling the coupling between vibrational excitation and dissociation must capture both the removal of vibrational energy due to dissociation and the slowing of dissociation due to vibrational nonequilibrium. Additionally, experiments with higher O_2 concentration will exhibit the influence of recombination on both vibrational energy and O_2 number density. Early theory from Hammerling *et al.* described how vibrational nonequilibrium slows dissociation.[38] This theory was later expanded upon by Marrone and Treanor to also include vibrational energy removal.[29,30] Together, this series of studies resulted in differential equations that describe coupled vibration-dissociation: one for the vibrational energy (E_v) and one for the number density of O_2 (n_{O_2}) [Eqs. (1) and (2)]. Unlike the highly dilute O_2–Ar model presented in Ref. 14, Eqs. (1) and (2) include the relevant terms for recombination reactions,

$$\frac{dE_v}{dt} = \frac{E_v^*(T_{tr}) - E_v(T_v)}{\tau(T_{tr})} + \frac{\varepsilon(T_v, T_{tr}) - E_v(T_v)}{n_{O_2}} \frac{dn_{O_2}}{dt}\bigg|_{diss.} + \frac{\varepsilon(T_{tr}, T_{tr}) - E_v(T_v)}{n_{O_2}} \frac{dn_{O_2}}{dt}\bigg|_{recomb.}, \tag{1}$$

$$\begin{aligned}\frac{dn_{O_2}}{dt} = &-k_d^{O_2-Ar}(T_{tr}) Z(T_v, T_{tr}) n_{O_2} n_{Ar} \\ &- k_d^{O_2-O_2}(T_{tr}) Z(T_v, T_{tr}) n_{O_2}^2 \\ &- k_d^{O_2-O}(T_{tr}) Z(T_v, T_{tr}) n_{O_2} n_O \\ &+ \frac{k_d^{O_2-Ar}(T_{tr})}{K_{eq}(T_{tr})} n_O^2 n_{Ar} + \frac{k_d^{O_2-O_2}(T_{tr})}{K_{eq}(T_{tr})} n_O^2 n_{O_2} \\ &+ \frac{k_d^{O_2-O}(T_{tr})}{K_{eq}(T_{tr})} n_O^3.\end{aligned} \tag{2}$$

Equation (1) describes the rate of change of the average vibrational energy per molecule of O_2 and includes transfer from translational modes to vibrational modes, vibrational energy loss through dissociation, and vibrational energy gain through recombination. The first term, representing the Bethe–Teller expression for vibrational relaxation, describes energy transfer from translational modes to vibrational modes, which depends on the equilibrium vibrational energy (E_v^*), the current vibrational energy (E_v), and the vibrational relaxation time (τ).[39] The second term describes the average vibrational energy loss due to dissociation, which depends on the dissociation rate ($\frac{dn_{O_2}}{dt}|_{diss.}$) normalized by the O_2 number density (n_{O_2}), the current vibrational energy (E_v), and the average energy loss (ε). Conversely, the third term describes the average vibrational energy gain due to recombination, which similarly depends on the recombination rate ($\frac{dn_{O_2}}{dt}|_{recomb.}$), n_{O_2}, E_v, and ε. In the case of dissociation, ε depends on both the vibrational temperature (T_v) and translational/rotational temperature (T_{tr}), because energy lost through O_2 dissociation depends on both the vibrational and translational energy of the O_2 molecules. However, in the case of recombination, ε only depends on T_{tr}, because the recombining collisions only involve the translational energy of O atoms. In the Marrone and Treanor theory, the same ε expression can

describe both dissociation and recombination, with recombination setting T_v equal to T_{tr}.[29,30] Together, these three terms account for the important pathways of vibrational energy transfer through vibrational relaxation, loss through dissociation, and gain through recombination.

Equation (2) describes the rate of change of O_2 number density for an O_2–Ar mixture undergoing dissociation and recombination reactions. The first three negative terms, expressed as $\frac{dn_{O_2}}{dt}|_{diss.}$ in Eq. (1), represent dissociation via collisions with Ar, O_2, and O, respectively, and each of these three dissociation reactions is characterized by a dissociation rate constant ($k_d^{O_2-Ar}$, $k_d^{O_2-O_2}$, or $k_d^{O_2-O}$), the vibrational coupling factor (Z), and the number densities of the two colliding species (n_{Ar}, n_{O_2}, or n_O). The remaining three positive terms, expressed as $\frac{dn_{O_2}}{dt}|_{recomb.}$ in Eq. (1), represent three-body recombination reactions again via collisions with Ar, O_2, and O. Unlike the three dissociation reactions, recombination reactions do not include a vibrational coupling factor, because the recombining O atoms do not carry vibrational energy. Instead, each of the three recombination reactions is characterized by a recombination rate constant, calculated by dividing the respective dissociation rate constant by the equilibrium constant (K_{eq}), and the number densities of the three colliding species. Values for K_{eq} were calculated using values from the NIST-JANAF thermochemical tables.[40] Together, these six terms account for the dissociation and recombination of O_2 for all possible collision partners in O_2–Ar mixtures.

The two coupling parameters, ε and Z, capture the removal of vibrational energy due to dissociation and the slowing of dissociation due to vibrational nonequilibrium. As such, both ε and Z are important targets for high-fidelity modeling of CVDV processes. Details of five models from Marrone–Treanor, Hansen, Kuznetsov, Ibraguimova, and Macheret–Fridman were previously described in Ref. 14 and are not repeated here.[1,25,29–34] However, the analysis of the Macheret–Fridman model was updated from a simplified model (Ref. 33) to the full model (Ref. 34). Recent quasi-classical trajectory (QCT) modeling by Chaudhry *et al.* has provided an additional model against which to compare experimental data.[1] This QCT-based model builds upon the framework of the Marrone–Treanor model to determine ε and Z by fitting QCT results to express the free parameter (U) as a function of the translational/rotational temperature (T_{tr}) [Eqs. (3)–(7)]. Because this model augments the Marrone–Treanor theory, the QCT-based model is referred to as the modified Marrone–Treanor (MMT) model,

$$\varepsilon_{MT} = \frac{k\theta_v}{\exp\left(\frac{\theta_v}{T_f}\right) - 1} - \frac{D_0}{\exp\left(\frac{D_0}{kT_f}\right) - 1}, \tag{3}$$

$$Z_{MT} = \frac{Q(T_{tr})Q(T_f)}{Q(T_v)Q(-U)}, \tag{4}$$

$$Q(T) = \frac{1 - \exp\left(-\frac{D_0}{kT}\right)}{1 - \exp\left(-\frac{\theta_v}{T}\right)}, \tag{5}$$

$$\frac{1}{T_f} = \frac{1}{T_v} - \frac{1}{T_{tr}} - \frac{1}{U}, \tag{6}$$

$$\frac{1}{U} = \frac{a_U}{T_{tr}} + \frac{1}{U^*}. \tag{7}$$

In Eqs. (3) and (4), the subscript (MT) denotes that these expressions for ε and Z arise directly from the original Marrone–Treanor theory. Both ε_{MT} and Z_{MT} are expressed in terms of known physical constants, two temperatures, and the free parameter (U). The physical constants include the Boltzmann constant (k), the dissociation energy (D_0), and the characteristic vibrational temperature (θ_v) [Eqs. (3) and (5)]. The model also uses the vibrational temperature (T_v) and translational/rotational temperature (T_{tr}), but it introduces a pseudotemperature (T_f) that combines T_v, T_{tr}, and U [Eq. (6)]. Notably, a truncated harmonic oscillator model is used for the vibrational partition function (Q) in the calculation of Z_{MT} [Eq. (5)]. Given the sign convention of the original Marrone–Treanor theory, positive values of U imply high-lying vibrational states dissociate with higher probability than the line-of-centers collision energy would predict. Equation (7) provides the major addition to Marrone–Treanor theory from the QCT modeling by Chaudhry *et al.*, and it demonstrates the MMT model recommendation to express U as a function of T_{tr} in terms of a slope parameter (a_U) and an intercept parameter (U^*). The values of a_U and U^* from the MMT model give positive values for U, which reflects the increased dissociation of high-lying vibrational states observed in the QCT results.

One advantage of using QCT methods in the development of the MMT model was that a large number of collisions with many combinations of initial translational, rotational, and vibrational energy were simulated using high-quality potential energy surfaces (PES).[1,41,42] By analyzing only those collisions that resulted in dissociation, the QCT results directly measured the probability that an O_2 molecule, originating in a particular vibrational energy level, would dissociate. As this probability formed the basis of the Marrone–Treanor model, the QCT results calculated ε for various combinations of T_v and T_{tr}. Finally, these results were compiled and fit to provide a recommended form for U in terms of T_{tr} and two fit parameters, a_U and U^* [Eq. (7)].

The MMT model does not restrict the vibrational energy levels to a Boltzmann distribution, and many of the high vibrational energy levels strongly deviate from a Boltzmann distribution.[1] However, the MMT model also proposes a simple correction factor to adjust the reaction rate and vibrational energy loss terms to account for non-Boltzmann behavior. The current experimental results are compared to the MMT model both with and without the non-Boltzmann correction.

C. Data analysis

Raw data from the experimental setup included the incident shock velocity from the five PCB pressure transducers, intensity signals from the four silicon optical detectors, and the pressure time-history from the Kistler pressure transducer. These raw data were subsequently analyzed to determine absorbance (α), pressure (P), vibrational temperature (T_v), translational/rotational temperature (T_{tr}), total O_2 number density (n_{O_2}), and state-specific number density ($n_{v''}$) time-histories. Subsequent analysis of the time-histories isolated the CVDV model parameters, including vibrational relaxation time (τ), average vibrational energy loss (ε), vibrational coupling factor (Z), and dissociation rate constants (k_d). Of the principal quantities of this work, α and P constitute the most direct measurements; T_v, n_{O_2}, and $n_{v''}$ were inferred from α spectroscopically; T_{tr} was simulated using energy conservation; and τ, ε, Z, and k_d were inferred from the temperature and number density time-histories [Eqs. (1) and (2)]. While

much of the current data analysis follows a similar procedure as that of the dilute O_2–Ar experiments, higher O_2 concentration experiments involved much larger T_{tr} and density (ρ) changes as a result of the endothermic vibrational relaxation and dissociation processes. The current data analysis procedure reflects the need to account for non-negligible density changes when inferring CVDV model parameters.

1. Calculation of time-histories

The procedure for calculating absorbance (α), vibrational temperature (T_v), translational/rotational temperature (T_{tr}), total O_2 number density (n_{O_2}), and state-specific number density ($n_{v''}$) time-histories follows the same steps for nondilute O_2 and O_2–Ar mixtures as it did for highly dilute O_2–Ar mixtures.[14,17] First, the absorbance time-history for each wavelength in a given shock experiment was calculated from the incident (I_0) and transmitted (I_t) light intensities using the Beer–Lambert relation, and laser intensity fluctuations were rejected via common-mode rejection [Eq. (8)],

$$\frac{I_t}{I_0} = \exp(-\alpha_\lambda) = \exp(-\sigma_\lambda(T_v, T_{tr}) n_{O_2} L). \tag{8}$$

The absorbance at a given wavelength (α_λ) is the product of the number density of O_2 (n_{O_2}), absorbing path length (L), and the absorbance cross section (σ_λ)—itself a function of T_v and T_{tr}. Leveraging the strong dependence of σ_λ on T_v, the T_v time-histories were calculated using the ratio of absorbances (R) at the two measured wavelengths (λ_1, λ_2), and this ratio was interpreted via the experimentally validated absorbance model [Eq. (9)]. Values for σ_λ and further details of the absorbance ratio can be found in Refs. 19 and 20,

$$R = \frac{\alpha_{\lambda_1}}{\alpha_{\lambda_2}} = \frac{\sigma_{\lambda_1}(T_v, T_{tr})}{\sigma_{\lambda_2}(T_v, T_{tr})}. \tag{9}$$

Having determined T_v, the n_{O_2} time-history was directly determined using the Beer–Lambert relation for either of the two wavelengths and the known values for α_λ, σ_λ, and L [Eqs. (8) and (10)],

$$n_{O_2} = \frac{\alpha_\lambda}{\sigma_\lambda(T_v, T_{tr}) L}. \tag{10}$$

Finally, the number density time-histories in specific vibrational levels ($n_{v''}$) were determined using their Boltzmann population fractions, which were calculated using T_v, the vibrational level energy ($E_{v''}$), the Boltzmann constant (k), and the vibrational partition function (Q) [Eqs. (5) and (11)],

$$\frac{n_{v''}}{n_{O_2}} = \frac{\exp\left(-\frac{E_{v''}}{kT_v}\right)}{Q(T_v)}. \tag{11}$$

For the high temperatures of this study, the assumption of a Boltzmann distribution likely breaks down for high-lying vibrational states, but the low-lying levels remain close to a Boltzmann distribution.[1,43–45] Since this study used wavelengths that probed $v'' = 5$ and 6, the population temperature based on the ratio of $v'' = 5$ and 6 closely matches the T_v describing all low-lying levels. Therefore, a Boltzmann distribution was deemed appropriate to calculate the state-specific number densities for $v'' = 5$ and 6.

Up to this point, the isolation of time-histories relied on the strong dependence of σ on T_v to justify neglecting T_{tr}. However, changes in T_{tr}, resulting from the endothermic vibrational relaxation and dissociation processes, influenced the density of the test gas, so the T_{tr} time-histories were simulated using the shock jump relations and applying energy conservation to a fluid mass element. The initial post-shock temperature (T_{tr}^0) was found using the measured incident shock velocity and assuming frozen chemistry and frozen energy in vibrational modes.[36] The assumption of frozen chemistry and frozen vibrational energy was justified by the low pressures and short time between incident and reflected shocks in these experiments. To ensure the evolving temperature change included both thermochemistry and pressure effects, the enthalpy change (dh) was calculated using the change in the measured pressure trace (dP) and the specific volume (v) [Eq. (12)]. Previous studies applied this same energy conservation method for an adiabatic system following a fixed mass element,[14–18,46]

$$dh = v dP. \tag{12}$$

The enthalpy was calculated with the NASA Glenn polynomials and leveraged the measured values for T_v and n_{O_2} [Eq. (12)].[47] The Glenn polynomials assume equilibrium between all energy modes, so contributions due to vibrational and electronic energy were adjusted to reflect experimental, nonequilibrium conditions by subtracting electronic and vibrational energy at T_{tr} and then adding the contributions at the measured vibrational and electronic temperatures, respectively. As recommended by the Park two-temperature model, the electronic temperature was assumed to equal the measured vibrational temperature.[48] Additionally, the measured n_{O_2} time-histories provided sufficient information to track the energy change from dissociation through the changing mole fractions of O_2, O, and Ar. The measured pressure, T_v, and n_{O_2} time-histories informed the non-ideal pressure rise, endothermic vibrational relaxation, and endothermic dissociation, respectively. Together, these three processes allowed the simulation of T_{tr} time-histories using the NASA Glenn polynomials.

2. Density change effects

While the absorbance, pressure, temperature, and number density time-histories—calculated for the laser observation location of 5 mm from the end wall—followed the same procedure as previous highly dilute O_2–Ar experiments, density change due to endothermic vibrational relaxation and dissociation required adjustments to the current procedure for isolating the CVDV coupling parameters.[14] Knowledge of the gas pressure, temperature, and composition helped determine the density time-histories for a given mass element. These density time-histories were then used to account for slight motion in the test gas due to density change by applying mass conservation. This motion in the test gas meant that the timing observed by the laser diagnostics—called lab time (t_{lab})—differed slightly from the timing experienced by the moving mass elements of reacting gas—called particle time (t_{part}).[15] The density increase from the endothermic reactions caused the gas to move slightly toward the end wall, thus causing the laser to observe a slightly different gas sample over time (Fig. 2). The gas that moves into the observation location was shock-heated at a slightly later time than the original gas, so it has undergone vibrational relaxation and dissociation for less time. For example, points A and C in Fig. 2 both represent observations of the laser diagnostics, and the time difference between them represents the lab time. However, density change causes point A to move out of the

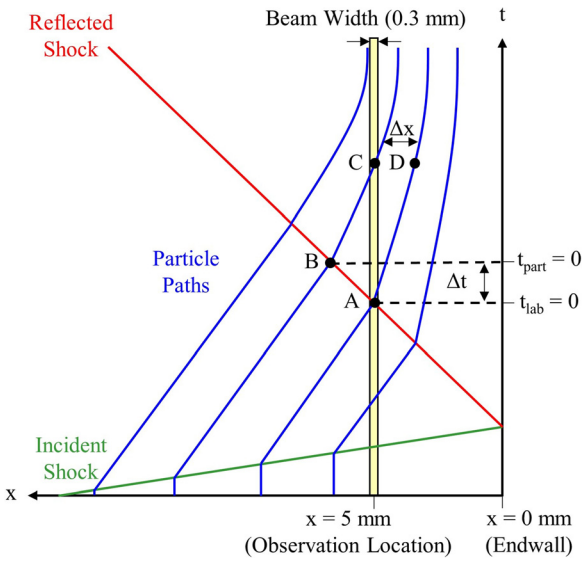

FIG. 2. Illustration of density change behind the reflected shock and the corresponding motion in the test gas. The conversion between lab time and particle time was needed to isolate CVDV rate parameters from the measured time-histories. This conversion was determined using the density time-history and conservation of mass.

observation location to point D. Instead, the observed particle at point C was originally shock-heated from a location further from the end wall at point B. The difference between the lab time and particle time (Δt) needed to be calculated to infer CVDV rate parameters—which manifest in the particle frame—from the time-histories—acquired in the lab frame.

To calculate the difference between lab time and particle time, mass conservation was applied for discrete mass elements by utilizing the density as a function of particle time. It was assumed that the adjacent mass elements sufficiently close to the measurement location were all shock-heated to approximately the same initial temperature (T_{tr}^0) and initial pressure (P^0). In this case, the density time-histories of all adjacent mass elements evolved the same in the particle frame, but the timing for each element was shifted based on when it was shock-heated. The density time-histories were used to track the motion of the particles by conserving the mass within each element and adjusting that element's thickness (Δx),

$$\Delta x_0 \rho_0 A = \Delta x(t_{part}) \rho(t_{part}) A. \tag{13}$$

In this case, the initial density (ρ_0) was known from the post-reflected-shock temperature, pressure, and composition, and the density time-history determined $\rho(t)$. The initial thickness (Δx_0) of the elements was chosen to be 0.1 mm to finely resolve the density change process. Ultimately, this provided a simple calculation to determine each mass element's thickness over time [Δx(t)], as the cross-sectional area of the shock tube (A) remained constant. Completing this calculation for the ensemble of mass elements and then summing the Δx(t) values, the overall position of each mass element could be calculated. Having determined the positions of a discrete set of mass elements, the timing difference (Δt) was calculated by tracing mass elements from 5 mm back to their starting position (x_0). Finally, the difference between lab time and particle time (Δt) was determined by dividing the distance between x_0 and 5 mm by the reflected shock velocity, U_{rs} [Eq. (14)],

$$\Delta t = \frac{x_0 - 5\text{mm}}{U_{rs}}. \tag{14}$$

Accounting for this motion provided the means to isolate CVDV rate parameters from the measured time-histories, though the density change correction was usually small. For example, an experiment with density increasing to twice its initial value—similar to the density changes in this study—would move particles to half their original distance from the end wall. In this case, the particles that end the experiment at 5 mm would have originated from 10 mm. Since the reflected shock velocities were approximately 1 mm/μs, this means Δt remained below 5 μs, even in the case of an extreme density change. Generally, the effect of gas motion decreases the closer the observation location is to the end wall. This study chose to measure at 5 mm to reduce the effect of gas motion while maintaining enough distance to neglect interactions with the end wall. Finally, the provided absorbance time-histories plot the best-fit simulation against both lab time and particle time to demonstrate the small difference.

3. Calculation of CVDV rate parameters

The measured time-histories, corrected from lab time to particle time, were fit to infer the CVDV model parameters. Similar to the dilute O_2–Ar experiments, certain portions of the time-histories were more sensitive to specific parameters than others, but unlike the dilute experiments, the large decrease in T_{tr} throughout the experiment slightly altered the fitting procedure.[14] Also unlike the dilute experiments, dissociation rate constants for all three collision partners—O_2, O, and Ar—were included in the fits.

The two temperature time-histories (T_v and T_{tr}) were used to calculate $E_v(T_v)$ and $E_v^*(T_{tr})$, respectively, and provided sufficient information to fit τ and ε. Approximately the first 5 μs of experimental test time were highly sensitive to τ only, so the vibrational relaxation time was isolated using the same methods outline in previous works.[14,18] Experiments were designed such that the approximate 5 μs of vibrational relaxation avoided the limitations of the 900 kHz optical detectors and the influence of shock thickness, shock curvature, beam thickness, or beam skew.[14] Because the dissociation for the first 5 μs was small, it was also straightforward to track the decrease in T_{tr} resulting in the measurement of $\tau(T_{tr})$. The contribution to τ due to collisions with O_2 ($\tau^{O_2-O_2}$) was separated from the Ar collisions (τ^{O_2-Ar}) and O collisions (τ^{O_2-O}) using the mole fractions (X_{O_2}, X_{Ar}, and X_O) and the mixture rule [Eq. (15)],[14]

$$\frac{1}{\tau^{mix}} = \frac{X_{O_2}}{\tau^{O_2-O_2}} + \frac{X_{Ar}}{\tau^{O_2-Ar}} + \frac{X_O}{\tau^{O_2-O}}. \tag{15}$$

The first two terms of Eq. (15) contributed strongly to the early-time relaxation, as there was not enough time for O atoms to form. This insensitivity to τ^{O_2-O} at early times ensured that $\tau^{O_2-O_2}$ could be inferred from data without major assumptions about O_2–O relaxation. However, determining ε from Eq. (1) at later times required addressing O_2–O vibrational relaxation. Generally, the mole fractions at any point of the time-history were inferred using the original mixture composition and measured O_2 number density throughout the experiment.

Additionally, the previous highly dilute experiments were leveraged for determining τ^{O_2-Ar}.[14] The current experiments were not sensitive enough to infer τ^{O_2-O} directly, so this work assumed a value for P τ^{O_2-O} of 4×10^{-8} atm-s. This value is approximately 50% larger than experimental data from Breen *et al.* and Keifer and Lutz, but neither set of experiments measured in the 4000–14 000 K range of these experiments.[49,50] Instead, the 4×10^{-8} atm-s value was chosen based on a survey of previous computational studies. The current value is most similar to the proposed expression from Ibraguimova *et al.*, but it also falls between calculated values from Grover *et al.* and Andrienko and Boyd.[25,43,51] Ultimately, a constant value for P τ^{O_2-O} was chosen to infer ε from Eq. (1), but this choice introduces uncertainty into the subsequent calculations.

Having assumed a constant value for P τ^{O_2-O}, ε was inferred from later portions of the temperature time-histories using Eq. (1). The rate of change of O_2 number density ($\frac{dn_{O_2}}{dt}$) was determined directly from the n_{O_2} time-histories, so ε remained as the only unknown in the second term. By additionally constraining the fit to between approximately 5 and 30 μs of experimental test time to minimize the influence of recombination, ε was fit directly from Eq. (1). After obtaining sufficient data across multiple experiments to provide an expression for $\varepsilon(T_v, T_{tr})$, this fitting procedure was refined to include recombination via $\varepsilon(T_{tr}, T_{tr})$. Leveraging the full set of experiments provided sufficient data to account for both vibrational energy loss due to dissociation and gain due to recombination while fitting for ε.

Once ε was inferred, Marrone and Treanor theory was used to relate ε and Z through the dissociation probability parameter, U [Eqs. (3)–(6)].[29,30] The same procedure was used to relate ε and Z in highly dilute experiments.[14] Isolation of Z from ε using Marrone and Treanor theory allowed both CVDV coupling parameters to be inferred from the measured T_v and simulated T_{tr} time-histories.

The results for ε and Z were highly dependent on the model used to calculate $E_v(T)$—as was the case in dilute experiments. This work calculated ε and Z using a simple harmonic oscillator model (SHO), an anharmonic oscillator model (AHO), the NASA Glenn polynomials (NASA), and the model values Rovibrational Energetics and Analysis of QuasiClassical Trajectories (REAQCT).[1,47,52] The SHO, AHO, and NASA models were previously described for the dilute O_2–Ar study, but the REAQCT model was added to this work to provide a fair comparison to the Modified Marrone–Treanor (MMT) model.[1,14] This work retains the results from the four models for $E_v(T)$ to demonstrate the scatter due to $E_v(T)$ model assumptions and to provide comparison options for computational models.

With the vibrational coupling factor, Z, determined, the dissociation rate constants (k_d) were inferred from the n_{O_2} time-histories [Eq. (2)]. The results from dilute experiments were leveraged to calculate $k_d^{O_2-Ar}$, while the remaining two dissociation rate constants, $k_d^{O_2-O_2}$ and $k_d^{O_2-O}$, were both inferred from the later portions of the time-histories.[14] First, $k_d^{O_2-O_2}$ was fit to the initial portion of the O_2 decay, where O atom concentration was negligible, while $k_d^{O_2-O}$ was fit toward the end of the test time where significant O atoms had formed. Additionally, the K_{eq} values from the NIST-JANAF thermochemical tables were leveraged to account for recombination reactions [Eq. (2)].[40] Though the fits for $k_d^{O_2-O_2}$ and $k_d^{O_2-O}$ overlapped, comparisons across experiments with multiple pressures, temperatures, and compositions helped to separate the two measurements. Overall, the experiments were more sensitive to $k_d^{O_2-O_2}$ even though both $k_d^{O_2-O_2}$ and $k_d^{O_2-O}$ were inferred from the n_{O_2} time-histories.

4. Best-fit absorbance simulation

The compiled results for τ, ε, Z, and k_d over the 6000–14 000 K temperature range provided sufficient data for a least squares curve fit giving expressions for $\tau(T_{tr})$, $\varepsilon(T_v, T_{tr})$, $Z(T_v, T_{tr})$, and $k_d(T_{tr})$, and the resulting expressions were subsequently used to simulate the experimental absorbance, thereby providing an additional comparison between CVDV rate parameter results and experimental time-histories. Besides a simple comparison between simulation and measurement, the best-fit absorbance simulation also provided the opportunity to perturb the CVDV rate parameters, thus determining the sensitivity of the absorbance time-histories to each CVDV rate parameter independently. Finally, these simulations were used to iterate on the density change calculation and the CVDV rate parameter fits to ensure convergence between simulation and experiment for all of the experimental conditions.

The absorbance time-history was simulated starting with the known post-shock temperatures (T_v^0 and T_{tr}^0) and the measured pressure [P(t)]. Combining the known starting condition with the expressions for $\tau(T_{tr})$, $\varepsilon(T_v, T_{tr})$, $Z(T_v, T_{tr})$, and $k_d(T_{tr})$, the evolution of E_v and n_{O_2} was then simulated via a forward Euler method with a time step of 0.08 μs [Eqs. (1) and (2)]. Each time step of this calculation also used energy conservation to determine T_{tr} and mass conservation to account for slight gas motion [Eqs. (12) and (13)].[47] This resulted in simulated values for T_v, T_{tr}, and n_{O_2} as well as providing the simulated difference between lab time and particle time (Δt). Finally, the simulated absorbance was calculated using the Beer–Lambert relation and the experimentally validated absorption cross section model [Eq. (8)].[19,20] Primarily, these absorbance simulations were a check to ensure that the inferred values for $\tau(T_{tr})$, $\varepsilon(T_v, T_{tr})$, $Z(T_v, T_{tr})$, and $k_d(T_{tr})$ reproduced the measured absorbance time-histories.

These simulated absorbance time-histories enabled the calculation of the sensitivity of the best-fit absorbance time-histories to each CVDV rate parameter. For this work, the absorbance sensitivity ($S_{\alpha,\beta}$) was quantified by independently perturbing each CVDV rate parameter (β) in the absorbance simulation by factors of two [Eq. (16)],

$$S_{\alpha,\beta} = \frac{d\alpha(t)}{d\beta}\frac{\beta}{\alpha(t)} \approx \frac{\alpha(t)|_{2\beta} - \alpha(t)|_{0.5\beta}}{2\beta - 0.5\beta}\frac{\beta}{\alpha(t)}. \tag{16}$$

This procedure is often used with chemical kinetics simulations to determine dominant chemical reactions over time for systems of many reactions. In a similar fashion, this work used sensitivity analysis to determine the dominant CVDV rate parameter for different portions of the experimental time-histories.

The quantified sensitivity was used to refine the procedure for fitting the CVDV rate parameters from experimental time-histories. The first attempt at fitting used estimates for the portion of the time-histories over which each parameter was fit, but the quantified sensitivity informed the adjustment of these fitting windows. Iterating between a best-fit absorbance simulation and the calculation of the CVDV rate parameters informed better fits and resulted in convergence between simulation and experiment over the various temperatures, pressures, and compositions studied.

5. Uncertainty analysis

The uncertainty in the measured time-histories arose from noise in the optical diagnostics, pressure transducers, and shock velocity

measurements and was propagated using a standard root-sum-squares method [Eq. (17)],

$$\gamma_\xi = \sqrt{\sum_{i=1}^{n} \left(\frac{d\xi}{dx_i}\bigg|_{x_i} \right)^2 \gamma_{x_i}^2}. \quad (17)$$

The uncertainty arising from the optical diagnostic and pressure transducer measurements was caused by electronic noise, so the standard deviation of the raw signal to the best-fit time-history determined the uncertainty for both absorbance and pressure. The absorbance best-fit was found using the aforementioned simulation of the CVDV process in tandem with an absorbance model.[20] In contrast, the pressure best-fit was obtained with a linear fit to the post-reflected-shock data. Additionally, the uncertainty in each of the four shock velocity measurements was propagated via the measured shock attenuation rate to calculate the initial post-reflected-shock temperature uncertainty. Next, the uncertainty in the O_2 vibrational temperature arose from the absorbance uncertainty but was amplified by the sensitivity of the absorbance ratio [Eq. (9)]. However, the wavelength selection and use of CW light were used to maximize the ratio sensitivity, thereby minimizing T_v uncertainty.[20] Finally, the uncertainty in the number density time-histories was propagated from the absorbance, pressure, and temperature uncertainties.

Unlike the time-histories, the CVDV coupling parameters—τ, ε, Z, and k_d—often involved nested exponential functions, hindering the expression of the partial derivatives in a simple, analytical form [Eqs. (1) and (2)]. Instead, these partial derivatives were approximated by perturbing the calculation by the uncertainty of each contributing parameter, and these approximated partial derivatives were then used for standard root-sum-squares error propagation. The only source of uncertainty for CVDV coupling parameters that were not captured using perturbation was the fitting uncertainty for the rate of change of E_v and n_{O_2}. Instead, least squares curve fits were used to calculate the 95% confidence interval, thereby determining the fitting uncertainty. By using perturbations and least squares curve fits, uncertainty was quantified for each of the five CVDV rate parameters studied.

III. RESULTS

The results of this study are divided into time-histories and CVDV rate parameters. Example time-histories for absorbance (α), pressure (P), temperature (T_v and T_{tr}), and number density (n_{O_2} and $n_{v''}$) are provided for pure O_2, 50% O_2–Ar, and 20% O_2–Ar experiments in Sec. III A and Appendix A. These measured time-histories demonstrate the quantum-state-specificity of the laser system, exhibit low uncertainty, and extend results to higher temperatures than previously achieved. In Sec. III B, plots demonstrate the time-dependent sensitivity of the best-fit absorbance time-history to the CVDV rate parameters, illustrating different early-time and late-time sensitivities. Finally in Sec. III C, the CVDV rate parameter results for vibrational relaxation time ($\tau^{O_2-O_2}$), average vibrational energy loss (ε), vibrational coupling factor (Z), and dissociation rate constants ($k_d^{O_2-O_2}$ and $k_d^{O_2-O}$) are plotted and compared to previous models and data.

A. Time-histories

Sections III A 1–III A 4 provide example time-histories for three experiments completed using 50% O_2 in Ar. Similar time-histories for three pure O_2 experiments and three 20% O_2–Ar experiments are provided in Appendix A.

1. Absorbance

Absorbance time-histories [α(t)] obtained from two UV laser diagnostics were measured at 223.237 nm and 236.9 nm for each of the pure O_2, 50% O_2–Ar, and 20% O_2–Ar experiments. The results for three 50% O_2–Ar are provided here, with three pure O_2 and three 20% O_2–Ar experiments provided in Appendix A (Figs. 3, 13, and 14). These example absorbance time-histories show the data quality, compare the best-fit absorbance simulations to the raw data, and illustrate the effect of gas motion on the simulated absorbance via the particle time simulations.

The measured absorbance time-histories demonstrate strong absorbance signals with relatively low noise (Fig. 3). The strength of the absorbance signals arose from both the strategic wavelength selection and the increased concentrations of O_2 in the test gas. In contrast, the magnitude of the laser noise was determined by the laser output power and the electronic noise in the silicon optical detectors. To partially mitigate this noise, the laser output power was maximized prior to each experiment, thereby decreasing the impact of the noise. Generally, the noise for the CW laser diagnostic, measuring at 223.237 nm, was slightly larger than the noise for the pulsed diagnostic, measuring at 236.9 nm. However, the extremely narrow spectral width of the CW laser diagnostic provided very strong sensitivity to the population in $v'' = 5$, partially mitigating the impact of the higher noise.[20] The combination of strong absorbance with low noise helped to maintain a consistently large signal-to-noise ratio (SNR), which directly corresponded to low absorbance uncertainty. Compared to the previous dilute O_2–Ar experiments, the strong SNR in this work showcases the diagnostic improvements.[14]

The best-fit simulations for the two wavelengths at each of the three temperatures demonstrate the agreement between the converged CVDV model parameter results and the raw absorbance measurement (Fig. 3). The plotted best-fit simulations represent the converged model parameter values after iterating upon parameter fits. Generally, the simulation and data agree to within the level of the raw absorbance noise, but in some regions the simulation deviates slightly from the raw data. This deviation is small and arises from using the full fit for the CVDV rate parameters instead of the individually measured values for each experiment. The good agreement between the best-fit absorbance simulation and the measured absorbance confirmed the CVDV rate parameter fits over the range of experimental conditions.

Finally, the converged best-fit simulation of absorbance was plotted against the particle time to show the difference between the measured time-histories in lab time and simulated time-histories in particle time (Fig. 3). Including both lab time and particle time provides options for both zero-dimensional modeling of the chemistry and one-dimensional modeling that accounts for the flow effects in a shock tube. The difference between lab time and particle time was smaller for lower temperatures and for higher Ar dilution because these experiments experienced smaller density changes. However, even high temperature, pure O_2 experiments exhibited only a small difference between lab time and particle time. The choice to measure at 5 mm significantly reduced the impact of test gas motion and

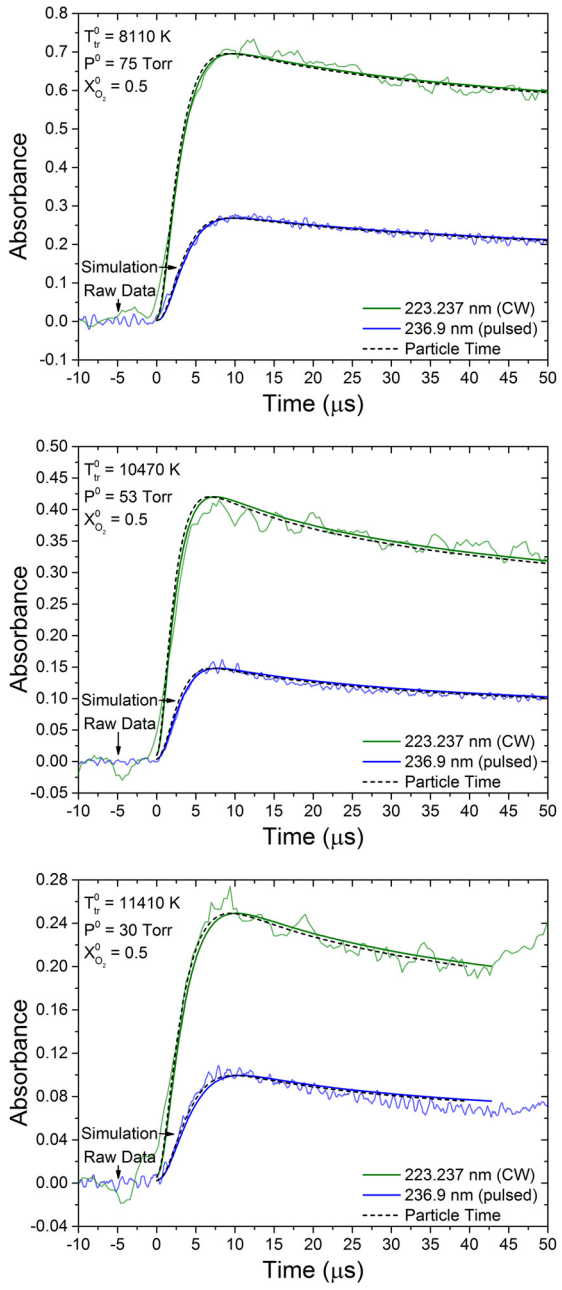

FIG. 3. Absorbance (α) time-histories for coupled vibration-dissociation shocks using 50% O_2 in Ar at three temperature conditions. The raw data demonstrate the relatively low noise of the two UV laser diagnostics, and the best-fit simulations show the good agreement between the converged CVDV simulations and raw data. The raw data and best-fit simulations are plotted against the lab time, but the best-fit simulations, replotted against the particle time, illustrate the small effect of density change and provide modeling options.

reduced the uncertainty of inferring CVDV rate parameters from the absorbance time-histories.

The current work improved the quality of the absorbance time-histories compared to past work by using improved diagnostics, extending test times with reflected shocks, and minimizing the influence of post-shock gas velocity. The narrow spectral output of the current laser diagnostics provided higher sensitivity to specific vibrational levels than broadband light sources, like those used by Ibraguimova *et al.*, thus providing a more sensitive measurement of vibrational temperature, number densities, and CVDV rate parameters.[25] Additionally, the use of reflected shocks resulted in higher time-resolution than using incident shocks, as in the Ibraguimova *et al.* work, by very nearly stagnating the test gas. For example, the highest temperature experiment from Ibraguimova *et al.*—10 820 K—had a lab-frame test time of 4 μs, whereas the 11 410 K experiment in Fig. 3 had a lab time of 40 μs—an order of magnitude longer. While test gas in the current work exhibited slight motion due to density change, the velocity of the test gas behind the reflected shock was much slower than the velocity behind the incident shock. Ibraguimova *et al.* also used a density correction for the analysis of the gas behind the incident shock, but the current use of reflected shocks reduced the magnitude of this correction while also extending the test times. By reducing the magnitude of the density correction, the current work also reduced the CVDV rate parameter uncertainty arising from the difference between lab time and particle time. In all, the optical strategies and use of reflected shocks were conducive to measuring low-noise absorbance time-histories with high time resolution at high temperatures.

2. Pressure

Pressure time-histories [P(t)] were measured in each shock experiment using a low-noise piezoelectric pressure transducer. An example time-history depicts the non-ideal pressure rise (dP/dt), demonstrates the relevant features of the incident and reflected shocks, and illustrates the magnitude of the pressure transducer noise (Fig. 4). Only one pressure time-history is provided, as each pressure time-history exhibits similar features. For reference, this example pressure

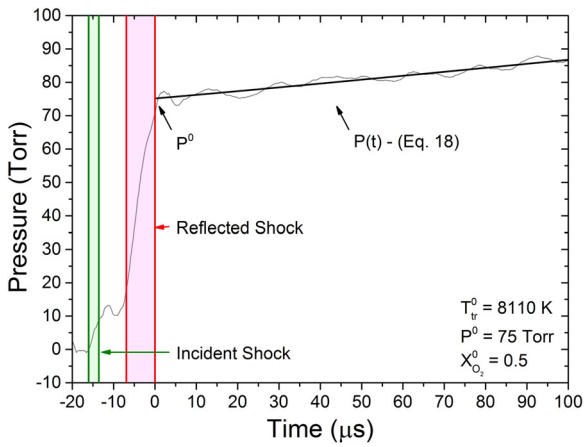

FIG. 4. Pressure (P) time-history for a 50% O_2–Ar experiment corresponding to the lowest temperature case in Fig. 3. The regions corresponding to the incident and reflected shock highlight the transit time of the shock across the 5.5 mm pressure transducer located 5 mm from the end wall. This case exhibited a non-ideal pressure rise ($\frac{dP}{dt}$) of 0.12 Torr/μs with $\frac{dP}{dt}$ ranging from 0.09 to 0.42 Torr/μs across this study [Eq. (18), Tables II–IV].

time-history corresponds to the lowest temperature absorbance time-history (Fig. 3).

The non-ideal pressure rise was typically linear, so this work used a simple linear fit to reduce the impact of transducer noise on the pressure time-history [Eq. (18)]. The values of initial post-reflected-shock pressure (P^0) and non-ideal pressure rise (dP/dt) for every experiment are tabulated in Appendix B (Tables II–IV),

$$P(t) = P^0 + \frac{dP}{dt}t. \tag{18}$$

In addition to showing the non-ideal pressure rise, Fig. 4 also highlights the regions corresponding to the incident and reflected shock. Though the incident and reflected shocks were very thin, the width of the pressure transducer resulted in finite transit times for each shock wave. As expected, the slower-moving reflected shock exhibits a longer transit time across the 5.5 mm diameter transducer—centered 5 mm from the end wall. Though this transit time affects the measured pressure time-histories, the laser beam waists were less than 1 mm, so the shock transit time did not strongly impact the absorbance, temperature, or number density time-histories.[14]

Finally, Fig. 4 demonstrates the magnitude of electronic noise for the pressure transducer measurement. Typically, the pressure noise remained within ±5% of the linear fit, and this variation was consistent regardless of initial pressure, P^0. Ultimately, the noise in the pressure measurement did not strongly contribute to the uncertainty in subsequent calculations.

3. Vibrational temperature

Vibrational temperature time-histories [$T_v(t)$] were obtained via the absorbance ratio, and translational/rotational temperature time-histories [$T_{tr}(t)$] were obtained via energy conservation [Eqs. (9) and (12)]. In this section, the results for three 50% O_2–Ar experiments are provided (Fig. 5), and these three cases correspond to the three 50% O_2–Ar absorbance time-histories (Fig. 3). Similarly, three pure O_2 and three 20% O_2–Ar temperature time-histories are provided in Appendix A (Figs. 15 and 16) and correspond to the included absorbance time-histories (Figs. 13 and 14). In all, the temperature time-histories demonstrate the sensitive measurement of T_v using UV laser absorption, exhibit a persistent depression of T_v below T_{tr} for 50% and 20% O_2–Ar mixtures, exhibit convergence of the two temperatures for the pure O_2 experiments, and show the large decrease in T_{tr} due to the endothermic vibrational relaxation and dissociation processes.

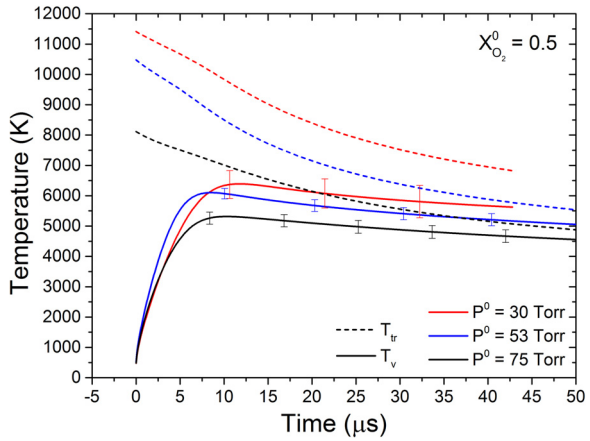

FIG. 5. Vibrational temperature (T_v) time-histories for three 50% O_2 in Ar experiments. The translational/rotational temperature (T_{tr}) time-histories were simulated using energy conservation and enthalpy values from literature [Eq. (12)].[47] The results demonstrate the sensitive measurement of T_v using two UV laser diagnostics. Finally, the observed depression of T_v below T_{tr} highlights the vibrational energy loss through dissociation.

The improved sensitivity of the current measurements, as compared to the dilute O_2–Ar experiments or the work by Ibraguimova *et al.*, arose from both the stronger, lower noise, absorbance signals and the use of a CW laser to measure at 223.237 nm.[14,25] The reduced absorbance uncertainty for each measured wavelength directly reduced the uncertainty in the absorbance ratio. Therefore, the improved absorbance measurements clearly and directly improved the sensitivity of the diagnostic measurement of T_v. However, the improved sensitivity achieved by using a CW laser to measure at 223.237 nm may be less immediately apparent. Previous studies that used light sources with broader spectra probed multiple transitions with contributions from multiple vibrational levels.[20,25] The narrow spectrum of the CW laser output light reduced the number of probed transitions, thereby increasing vibrational-state-specificity. The combination of strong absorbance signals with an inherently more sensitive diagnostic improved the measurement of T_v time-histories (Fig. 5).

The higher O_2 concentrations maintained low uncertainty throughout the test time, which was not the case for dilute O_2–Ar experiments.[14] Even if the reaction were to proceed to equilibrium, the current mixtures contained enough O_2 to make low-uncertainty measurements of T_v. For the pure O_2 and 50% O_2–Ar experiments, even the highest temperature conditions retained enough O_2 for low-uncertainty measurements (Figs. 3, 5, 13, and 15). However, the uncertainty for the highest temperature 20% O_2–Ar experiments increased over time because the nearly complete dissociation strongly reduced the absorbance signals (Figs. 14 and 16). Overall, the persistence of strong absorbance signals improved the T_v time-history measurements by maintaining low uncertainty throughout the test time.

The current results exhibit a persistent depression of T_v below T_{tr} for the 50% and 20% O_2–Ar experiments (Figs. 5 and 16). The depression in the diluted experiments was expected from the CVDV framework, because the dissociation of O_2 removes vibrational energy, thus suppressing the increase in T_v due to vibrational relaxation.[29,30,38] A similar depression was also observed in the highly dilute O_2–Ar experiments.[14] Recombination reactions later add vibrational energy for diluted O_2–Ar mixtures, thereby resulting in the eventual convergence of T_v and T_{tr} at equilibrium. However, the measured T_v time-histories in 50% and 20% O_2–Ar mixtures were not measured for a long enough time for the recombination reactions to converge T_v and T_{tr}, so the depression of T_v below T_{tr} persisted for the full experimental test time. Overall, this depression of T_v below T_{tr} in diluted experiments remains consistent with previous experimental results and highlights an important aspect of the CVDV processes.[14,18]

Unlike the diluted experiments, T_v and T_{tr} were observed to converge in the pure O_2 experiments (Fig. 15). A persistent depression of T_v below T_{tr} requires dissociation to remove vibrational energy faster than it can be replenished through vibrational relaxation, which is the case for O_2–Ar mixtures. However, the pure O_2 experiments produce

significantly more O atoms, and O_2–O vibrational relaxation occurs very fast.[25,43,49–51] The higher prevalence of O atoms—with their associated fast vibrational relaxation—likely explains the convergence of T_v and T_{tr} in the pure O_2 experiments compared to the persistent depression observed in the 50% and 20% O_2–Ar experiments.

The temperature time-histories in Fig. 15 can be compared to those measured by Ibraguimova *et al.* in pure O_2.[25] The Ibraguimova experiments also observed a convergence between T_{tr} and T_v within their experimental test time, but their measured peak values for T_v are up to 1000 K larger than those of this study for similar initial temperatures (T_{tr}^0). The peak value provides a useful comparison between the two sets of experiments because the experimental timing differs between the current experiments and the Ibraguimova *et al.* experiments. Primarily, this timing difference arises from the difference between incident and reflected shock experiments, but the lower pressures in the current experiments also extend the time for vibrational relaxation and dissociation. Considering the Ibraguimova experiments retain uncertainty of roughly ±1000 K, the current work may still agree to within experimental uncertainty for the peak values of T_v. The current experiments exhibit reduced T_v uncertainty due to the sensitive UV laser diagnostics, but the data still exhibit some consistency with the previous Ibraguimova *et al.* experiments.

The simulated T_{tr} decreased significantly due to the endothermic vibrational relaxation and dissociation process over the experimental test times. Higher temperature experiments exhibited a much larger decrease in T_{tr} due to the greater extent of vibrational excitation and dissociation. Similarly, higher O_2 concentration experiments exhibited a larger decrease in T_{tr} due to the greater influence of the endothermic dissociation. Tracking the decrease in T_{tr} for each experiment was an integral step in the calculation of density change and therefore the simulation of test gas motion. Finally, the measured T_v time-histories and simulated T_{tr} time-histories were used to track the CVDV rate parameters as functions of temperature, thereby assisting in the parameter fits for $\tau(T_{tr})$, $\varepsilon(T_v, T_{tr})$, $Z(T_v, T_{tr})$, and $k_d(T_{tr})$.

4. Number densities in specific vibrational levels

Total O_2 number density time-histories [$n_{O_2}(t)$] were calculated using the measured absorbance, the measured temperatures, and the Beer–Lambert relation [Eq. (8)]. Then, vibrational-state-specific number density time-histories [$n_{v''}(t)$] were calculated using a Boltzmann distribution [Eq. (11)]. As was the case for the other time-history results, only 50% O_2–Ar results are given in this section with the pure O_2 and 20% O_2–Ar results included in Appendix A (Figs. 6, 17, and 18). The provided number density time-histories highlight the quantum-state specificity of the two UV laser absorption diagnostics, demonstrate the competing effects of density increase and dissociation on $n_{O_2}(t)$, and display the low uncertainty of these measurements.

The measurement of populations in $v'' = 5$ and 6 exemplifies the quantum-state specificity of the UV laser absorption diagnostics (Fig. 6). Though a Boltzmann distribution was used to calculate $n_{v''}(t)$ from $n_{O_2}(t)$, the specific wavelengths chosen for this study were especially sensitive to the $v'' = 5$ and 6 populations.[19,20] These state-specific number density time-histories increase at early times as the excited vibrational levels are populated through vibrational relaxation. Subsequently, the state-specific number density time-histories reach a peak before declining due to dissociation. These quantum-state-specific number density results provide valuable, high-temperature validation data for computational models.

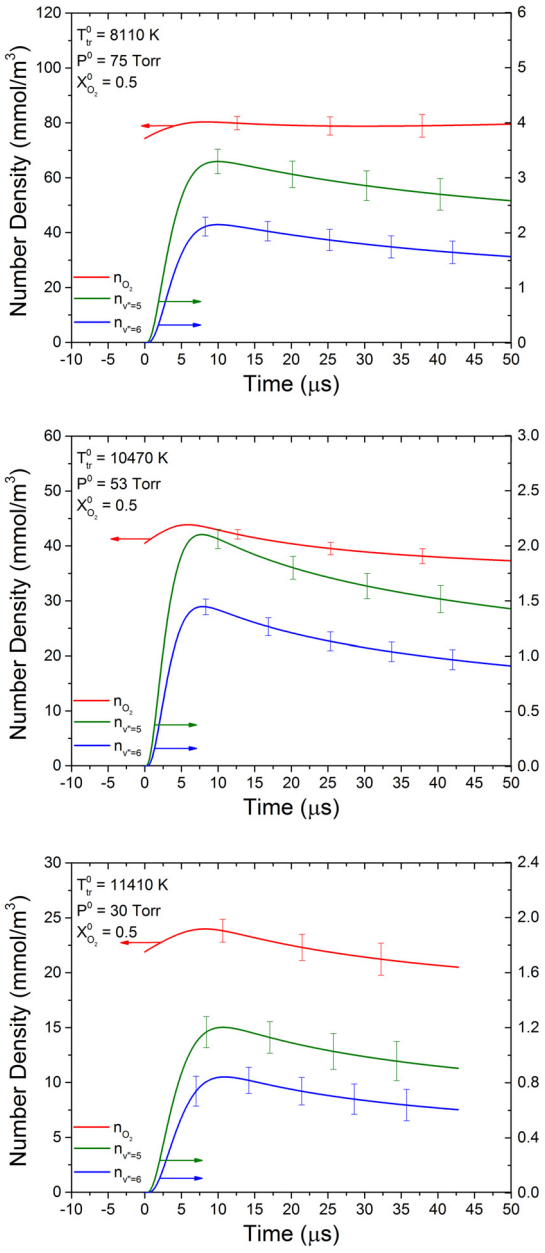

FIG. 6. Number density time-histories for the total amount of O_2 (n_{O_2}) and for specific vibrational levels ($n_{v''}$) measured in three 50% O_2 in Ar experiments. Although O_2 dissociates, n_{O_2} remains fairly constant due to the strong decrease in T_{tr}. However, the populations in $v'' = 5$ and 6—measured at 223.237 nm and 236.9 nm, respectively—evolve due to both dissociation and the change in T_v [Eq. (11)]. These results demonstrate the low uncertainty and the quantum-state specificity of the laser diagnostics.

The total O_2 number density time-histories exhibit different behavior than the state-specific time-histories because of the competing effects

of density increase and dissociation. Large changes in T_{tr} caused the total gas number density, n(t), to increase significantly over the test time. This effect was most apparent for the pure O_2 time-histories (Fig. 17). However, dissociation caused $n_{O_2}(t)$ to decrease relative to the increase in n(t) as O_2 reacted to form O atoms. The effect of dissociation was more apparent for the 20% O_2–Ar time-histories, as T_{tr} changed less (Fig. 18). Though each n_{O_2} time-history exhibited the competing effects of density increase and dissociation, the effects were more balanced for the 50% O_2–Ar experiments, thereby resulting in relatively constant n_{O_2} throughout the experimental test time (Fig. 6).

Note that the Boltzmann distribution used to calculate $n_{v''}$ assumed that all of the O_2 was in the electronic ground state ($X^3\Sigma_g^-$) [Eq. (11)]. This reflects an assumption typically made in computational modeling approaches, but the low-lying electronic states of oxygen ($a^1\Delta_g$ and $b^1\Sigma_g^+$) may play an important role in the energy transfer.[21,22,53] If the electronic energy modes are instead assumed to be in equilibrium with the vibrational modes as is assumed in the Park two-temperature model, the values for $n_{v''}$ in the electronic ground state would decrease by 5%–15%. The experimental uncertainty for $n_{v''}$ typically spans ±10%–15%, so the decrease due to population in the low-lying electronic states would still mostly remain within the uncertainty bounds.

The uncertainty in $n_{O_2}(t)$ and $n_{v''}(t)$ increased at higher temperatures but decreased with higher oxygen concentrations, and both factors were affected by the signal-to-noise ratio of the absorbance measurements (Fig. 6). The magnitude of the experimental uncertainty remained fairly constant over the experimental test times because the absorbance and temperature uncertainties also remained fairly constant (Figs. 3 and 5). Again, the exception was the highest temperature 20% O_2–Ar experiments, which exhibited increased uncertainty where the absorbance approached zero (Figs. 14 and 18). The reduced uncertainty, compared to the previous dilute O_2–Ar experiments, demonstrates the benefit of strong absorbance signals and increased T_v sensitivity of the UV laser diagnostics.

B. Time-history sensitivity to CVDV rate parameters

Sensitivity of the simulated, best-fit absorbance time-histories to each CVDV rate parameter was calculated by separately perturbing each CVDV rate parameter in the simulation by factors of two [Eq. (16)]. The sensitivity calculations did not consider the sensitivity to $k_d^{O_2-Ar}$, τ^{O_2-Ar}, or Z because the O_2–Ar rates were previously measured and Z was determined from ε using Marrone and Treanor theory. However, the calculations do include the sensitivity to τ^{O_2-O} since an assumed value was used for the analysis. The three plotted conditions were selected because they have roughly the same initial temperature (T_{tr}^0) but in mixtures of pure O_2, 50% O_2–Ar, and 20% O_2–Ar (Fig. 7). Each of the plotted sensitivity calculations also corresponds to a provided absorbance time-history (Figs. 3, 13, and 14). Together, these three sensitivity calculations illustrate the impacts of CVDV rate parameters on the simulated absorbance time-histories, demonstrate the effect of mixture composition on the ability to infer CVDV rate parameters, and exemplify the regions of the absorbance time-histories best suited for inferring specific CVDV rate parameters.

The sensitivity quantifies how a small change in one of the CVDV rate parameters would change the simulated absorbance time-history. As such, the negative values for these sensitivity calculations show that increasing any of the CVDV rate parameters would decrease

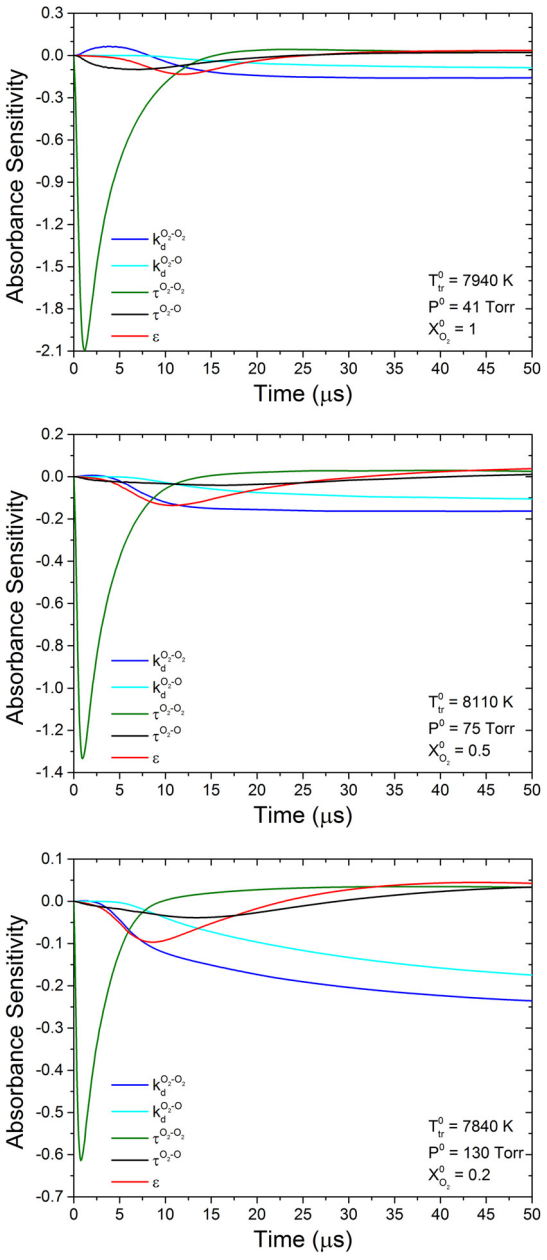

FIG. 7. Sensitivity of the absorbance best-fit simulation to each of the independent coupling parameters ($\tau^{O_2-O_2}$, τ^{O_2-O}, ε, $k_d^{O_2-O_2}$, and $k_d^{O_2-O}$) for three mixtures with approximately the same initial temperature. Primarily, $\tau^{O_2-O_2}$ strongly influences simulated absorbance at early times, whereas the other parameters all influence simulated absorbance at later times. Finally, the sensitivity to $\tau^{O_2-O_2}$ strongly decreases with lower O_2 mole fraction, while the sensitivity to the other three parameters remains fairly constant.

the simulated absorbance—as expected from the CVDV model. For example, increasing $\tau^{O_2-O_2}$ or τ^{O_2-O} results in the slower population of the excited vibrational states, and lower population in these states corresponds directly to lower absorbance. Similarly, increasing ε

suppresses the population in the absorbing state by removing vibrational energy, and increasing $k_d^{O_2-O_2}$ or $k_d^{O_2-O}$ suppresses the population by decreasing the overall population of O_2. The magnitude of the sensitivity also relates the uncertainty of the absorbance time-history to the uncertainty in the CVDV rate parameter fit. A larger value for the sensitivity corresponds to lower uncertainty for the CVDV rate parameter fit. As a result, the CVDV rate parameters were fit to portions of the time-histories with the largest magnitude of absorbance sensitivity.

A comparison across the three mixtures reveals the diminishing sensitivity of early-time absorbance measurements to $\tau^{O_2-O_2}$ with diminishing O_2 mole fraction, whereas the sensitivity to $k_d^{O_2-O_2}$, $k_d^{O_2-O}$, and ε remains of similar magnitude (Fig. 7). The mixture rule for vibrational relaxation time explains the diminishing sensitivity to $\tau^{O_2-O_2}$ as X_{O_2} decreases [Eq. (15)]. The magnitude of sensitivity to $k_d^{O_2-O_2}$, $k_d^{O_2-O}$, and ε all peak at similar values, but the time-dependent behavior of each mixture differs somewhat. These differences in the time-dependent behavior arise because the 50% O_2–Ar and 20% O_2–Ar experiments have higher pressure and do not undergo as large decreases in T_{tr} as 100% O_2 experiments, and both factors result in the diluted mixtures approaching equilibrium faster. Overall, these sensitivity plots highlight how Ar dilution changes the absorbance sensitivity to the CVDV rate parameters.

Despite diminishing sensitivity over the experimental test time, $\tau^{O_2-O_2}$ clearly controls the absorbance sensitivity of the first 5 μs of experimental test time, thereby justifying an early-time fit for isolating $\tau^{O_2-O_2}$. The late-time absorbance behavior retains sensitivity to $k_d^{O_2-O_2}$, $k_d^{O_2-O}$, and ε. Separating these three parameters required the n_{O_2} time-history measurement. The direct measurement of $n_{O_2}(t)$ provided enough information to solve for ε from Eq. (1) without needing to assume values for $k_d^{O_2-O_2}$ or $k_d^{O_2-O}$. By using ε to calculate Z, $k_d^{O_2-O_2}$ and $k_d^{O_2-O}$ were both subsequently inferred from $n_{O_2}(t)$ [Eqs. (2)–(6)]. However, the absorbance sensitivity demonstrates the higher sensitivity of the best-fit absorbance simulations to $k_d^{O_2-O_2}$ and the earlier onset of this sensitivity in the time-history. Taking advantage of this sensitivity difference provided the means to individually isolate $k_d^{O_2-O_2}$ and $k_d^{O_2-O}$. The time-dependent nature of the sensitivity calculations allowed the refinement of the CVDV rate measurements by iterating and adjusting the fitting windows.

Finally, the sensitivity to τ^{O_2-O} was included to illustrate the slight impact of this parameter on the absorbance simulations. In these calculations, the value for τ^{O_2-O} was also perturbed by factors of two from its assumed constant value of 4×10^{-8} atm-s, but the studies from which it was estimated have a spread of almost a full order of magnitude at high temperature. Based on the plotted values, sensitivity to τ^{O_2-O} is largest for the pure O_2 experiment, and this corresponds to the greater formation of O atoms in pure experiments. Only in the pure experiments does the sensitivity to τ^{O_2-O} reach similar values as those of the other four parameters. In fact, the sensitivity to τ^{O_2-O} in the 50% and 20% O_2–Ar experiments was mostly negligible. The inference of ε and Z from data required a value for τ^{O_2-O}, but it is reassuring that the absorbance simulations were not significantly sensitive to the assumed value.

C. Coupled vibration-dissociation rate parameters

Sections III C 1–III C 4 provide plots for each of the five measured CVDV rate parameters and compare the current results to previous data and models. Tabulated values for the plotted data and corresponding experimental conditions are provided in Appendix B.

1. Vibrational relaxation time

Vibrational relaxation time results for O_2–O_2 collisions ($\tau^{O_2-O_2}$) were inferred from fits to $T_v(t)$ at early times and extend the measurements to 14 000 K—a higher temperature than any previous study (Fig. 8). While the current study achieved slightly higher temperature for pure O_2 experiments than a previous study by the authors, diluted mixtures of 50% O_2–Ar and 20% O_2–Ar were leveraged for access to the highest temperatures.[18] However, Ar dilution also introduced the need to apply the mixture rule, so τ^{O_2-Ar} was extracted from a best-fit to previous 2% and 5% O_2–Ar experimental data [Eq. (19)].[14] The

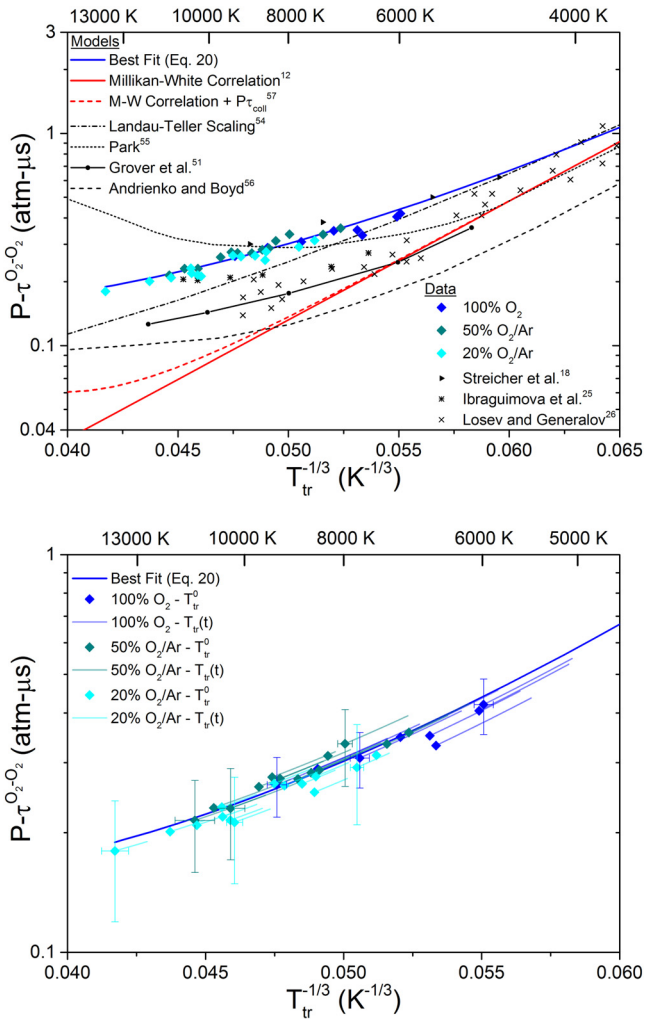

FIG. 8. Landau–Teller plots depicting $\tau^{O_2-O_2}$ as a function of T_{tr}. The first plot provides a comparison of the current data to literature data and models.[12,18,25,26,51,54–57] Data points are plotted with the initial temperature, T_{tr}^0, and the lines in the second plot denote how $\tau^{O_2-O_2}$ evolved as temperature decreased. For the 50% O_2–Ar and 20% O_2–Ar experiments, $\tau^{O_2-O_2}$ was isolated using the mixture rule and τ^{O_2-Ar} results from prior work [Eqs. (15) and (19)].[14]

current $\tau^{O_2-O_2}$ results exhibit reasonable self-consistency across the pure O_2, 50% O_2–Ar, and 20% O_2–Ar data, demonstrate the low-uncertainty of the measurements, resolve $\tau^{O_2-O_2}$ as a function of T_{tr}, and show a reduced temperature dependence at high temperatures compared to the dependence shown in previous data and models

$$P\tau_{BF}^{O_2-Ar} = 4.7\times10^{-9}\times\exp\left(\frac{200}{T_{tr}^{1/3}}\right)\times\frac{T_{tr}^{5/6}}{1-\exp\left(-\frac{2240}{T_{tr}}\right)}, \quad (19)$$

$$P\tau_{BF}^{O_2-O_2} = 8.4\times10^{-9}\times\exp\left(\frac{170}{T_{tr}^{1/3}}\right)\times\frac{T_{tr}^{5/6}}{1-\exp\left(-\frac{2240}{T_{tr}}\right)}. \quad (20)$$

The $\tau^{O_2-O_2}$ results not only demonstrate self-consistency, but remain largely consistent with previous results obtained in pure O_2 experiments in Ref. 18. In fact, the overlap between the current study and Ref. 18—which used only the pulsed UV laser—was sufficient to support only a slight modification to the pre-exponential constant in the best-fit equation [Eq. (20)]. Reference 18 used a constant of 8.9×10^{-9}atm-μs, while the current work uses 8.4×10^{-9}atm-μs. However, both the current best-fit and Ref. 18 best-fit fall within the experimental uncertainty for all experiments. The current data show very slight clustering among the pure O_2, 50% O_2–Ar, and 20% O_2–Ar results, respectively, but this clustering remains smaller than the uncertainty of any given experiment. The clustering may arise from small errors in τ^{O_2-Ar} or the conversion between particle time and lab time, but the overall scatter only spans ±10% while the typical uncertainty for any given experiment is ±25%. The current uncertainty is slightly lower than that of Ref. 18 because of the introduction of the CW laser system and the subsequent improvement of the T_v time-history uncertainty.

Discussion of the previous data from Refs. 25 and 26 was provided in Ref. 18 as well as discussion of the previous models (Refs. 12, 51, and 54–56). However, the current work also provides a comparison to the collision-time correction of the Millikan and White correlation, which was discussed for τ^{O_2-Ar} in Ref. 14.[56] The collision-time correction was added because the modified Marrone and Treanor (MMT) model uses the corrected Millikan and White correlation for $\tau^{O_2-O_2}$.[1]

As in Ref. 18, the results for $\tau^{O_2-O_2}$ deviate very strongly from the Millikan and White correlation at high temperatures—even with the collision-time correction.[12,56] Additionally, the current results measured longer relaxation times than the predictions of quasi-classical trajectory (QCT) model by Grover *et al.* and the forced harmonic oscillator (FHO) model by Andrienko and Boyd.[51,56] For the QCT model, the discrepancy may arise from allowing O_2 molecules to occupy energies that do not correspond to actual rovibrational quantum states.[51] For the FHO model, the discrepancy possibly arises from excluding higher-order terms in the Landau–Teller theory for vibrational relaxation.[56] The current results show some consistency with the semiempirical correction developed by Park and the scaling from higher-order terms developed by Landau and Teller, but neither captures the highest temperature behavior.[54,55] Finally, the current results measured longer relaxation times than previous experiments, though the current work demonstrates stronger absorbance signals, narrower spectral width of the probing light, and longer rise times than the previous experiments.[25,26] In particular, Refs. 25 and 26 fit $\tau^{O_2-O_2}$ from approximately 0.2–0.5 μs behind incident shocks, so the finite extent of the shock wave, test gas motion, or density change effects could explain the discrepancy. The large spread among previous models and data demonstrates the value of the low scatter and uncertainty in the current high-temperature $\tau^{O_2-O_2}$ measurements.

2. Average vibrational energy loss

The average vibrational energy loss due to dissociation (ε) was inferred from late-time fits of Eq. (1) using the measured values for T_v, T_{tr}, and n_{O_2}. The plotted and tabulated results normalize $\varepsilon(T_v, T_{tr})$ by the dissociation energy (D_0) (Fig. 9). This work used a D_0 value of 494 kJ/mol, which corresponds to the value found for the Arrhenius fit of $k_d^{O_2-O_2}$. Most of the models do not specify a value for D_0, so 494 kJ/mol was also used to normalize the model results—with the exception of the modified Marrone and Treanor model, which inferred a D_0 value of 503 kJ/mol from the QCT data.[1] Additionally, the results were calculated using four models for vibrational energy [$E_v(T)$].[1,47,52] For clarity, Fig. 9 only plots all four models for the highest and lowest temperature conditions, but the full data for each model is included in Table VII in Appendix B. The anharmonic oscillator (AHO) results were plotted for all temperatures because this model better reflects the values used in the spectroscopic model.[19,20,52] Model values were calculated at the measured T_v and simulated T_{tr} for comparison with experimental data. Overall, the ε results exhibit some clustering based on mixture composition and follow the same trend as the modified Marrone and Treanor (MMT) model, although they deviate in magnitude from the MMT model predictions.

The very slight clustering of ε for the three mixture compositions may stem from the use of a single ε regardless of collision partner [Eq. (1)]. While the use of a single ε was appropriate for highly dilute O_2–Ar experiments where nearly every collision was O_2–Ar, pure O_2, 50% O_2–Ar, and 20% O_2–Ar mixtures may need to account for

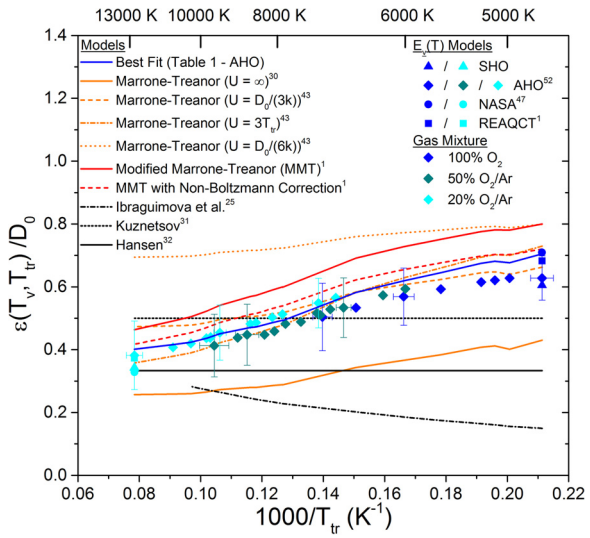

FIG. 9. Average vibrational energy loss (ε) as a function of translational/rotational temperature (T_{tr}). Each data point has a corresponding vibrational temperature (T_v) specified in Appendix B. The highest and lowest temperature conditions show ε calculated using four models for $E_v(T)$.[1,47,52] Although the results are compared to multiple models, the experimental results trend most similarly to the MMT model for O_2–O_2 with non-Boltzmann correction.[1,25,30–32,43]

different vibrational energy loss terms for each of the O_2–Ar, O_2–O_2, and O_2–O dissociating collisions. The recent MMT model provides separate fits of ε for both O_2–O_2 and O_2–O dissociating collisions (Table I).[1] Treating ε as collision partner dependent may better reflect the processes for the current high O_2 concentration experiments. Unfortunately, the current diagnostics do not provide the sensitivity to resolve separate ε for each collision partner, and instead a single ε was inferred for each experiment. While unable to resolve the collision partner dependence, the current ε results still provide a novel comparison to CVDV models that retains relatively low uncertainty.

The MMT model presents a convenient form in which to fit ε by manipulating the free parameter (U) [Eqs. (3)–(7)].[1] A fit of this form, for each of the four E_v(T) models, reasonably captured the behavior of the experimental data (Fig. 9). For clarity and consistency with the plotted data, only the fit for the anharmonic oscillator (AHO) model is plotted—in blue—in Fig. 9, but fit parameters for all four models are presented in Table I. Meanwhile, the solid red line in Fig. 9 plots the O_2–O_2 results from the MMT model for ε, but Table I also specifies the fit parameters for the O_2–O fit.[1] Notably, the slope parameter (a_U) for the MMT model has values similar to the experimental fits, but the intercept parameter ($1/U^*$) differs somewhat. This corresponds to the similarity in trend but different values seen in Fig. 9. The MMT model fits are more similar to the NASA and REAQCT fits than the AHO or SHO fits. Finally, the dilute O_2–Ar experiments from Ref. 14 were retroactively fit using the MMT model form, and this fit is also included in Table I.

The data span the two constant-value models by Hansen and Kuznetsov, and while these models express the ε simply, they oversimplify the energy loss process.[31,32] Meanwhile, the empirical model by Ibraguimova, fit to data above 7000 K, trends very differently than the others.[25] The Ibraguimova *et al.* experiments were completed in a 4000–10 800 K range, so Fig. 9 only plots the model below 10 800 K.

The experimental data consistently fall between the MMT model and the Marrone and Treanor model calculated with $U = \infty$.[1,30] $U = \infty$ implies that the probability of dissociation from each vibrational state only depends on the state's fractional population—defined using T_v—and the line-of-centers collision energy—defined using T_{tr}.[1,14,30] Conversely, the positive, but finite, values of U in the MMT model imply high-lying states dissociate with higher probability than predicted via the line-of-centers collision energy. As described in Ref. 43, $U = D_0/(3k)$, $U = 3T_{tr}$, and $U = D_0/(6k)$ are common empirical values to account for the high vibrational state dissociation for the original Marrone and Treanor model. Of these three empirical values for U, $U = D_0/(3k)$ and $U = 3T_{tr}$ overlap with the current data, though $U = D_0/(6k)$ exceeds the current data and other models. The current data suggest an impact on dissociation from high-lying vibrational states, but scatter among the E_v(T) models obscures the appropriate correction to account for high-lying states. For example, the AHO model predicts a smaller influence of high-lying states than the MMT model prediction, but the MMT model and REAQCT model predict similar corrections.

TABLE I. Current experimental best-fit MMT model parameters for various vibrational energy calculations [Eq. (7)].[1,47,52] Chaudhry *et al.* MMT model parameters for O_2–O_2 and O_2–O collisions are included for comparison.[1] The final value provides the experimental best-fit MMT model parameters for the previous dilute O_2–Ar experiments.[14]

Model	a_U	$1/U^*$ (K^{-1})
SHO	0.2	7×10^{-6}
AHO[52]	0.2	2×10^{-5}
NASA[47]	0.3	5×10^{-6}
REAQCT[1]	0.3	2×10^{-6}
MMT: O_2–O_2[1]	0.3965	1.7×10^{-5}
MMT: O_2–O[1]	0.3537	4.2×10^{-6}
O_2–Ar[14]	0.4	-7×10^{-5}

For all four E_v(T) models, the MMT model with non-Boltzmann correction results in reasonable agreement with experimental data. In particular, the MMT model with non-Boltzmann correction falls within the uncertainty bounds of nearly all experimental data regardless of E_v(T) model. The non-Boltzmann correction reconciles the appropriate Boltzmann distribution describing the low-lying vibrational states with the non-Boltzmann behavior of the high-lying vibrational states. The current experiments only probed low-lying vibrational states ($v'' = 5$ and 6) and were unable to probe the non-Boltzmann behavior of high-lying states, thus the MMT model with non-Boltzmann correction more accurately reflects the interpretation of the experimental data.

Ultimately, the most consistent comparison is between the MMT model with non-Boltzmann correction and the experimental data calculated with the REAQCT model for E_v(T). The same QCT results provide the foundation for both the REAQCT and MMT models, so using the REAQCT model while inferring the experimental data better reflects the MMT model values.[1] The good agreement between the experimental data and MMT model, both using the REAQCT model, highlights the importance of comparing experiments and models using consistent models for E_v(T).

3. Vibrational coupling factor

The vibrational coupling factor (Z) was calculated directly from ε using Marrone and Treanor theory [Eqs. (3)–(7)].[30] Therefore, the trends of the Z results and comparisons to models follow similar behavior as was observed for ε. Again, the results were calculated using four models for vibrational energy [E_v(T)], but Fig. 10 only plots all four models for the highest and lowest temperature conditions for clarity.[1,47,52] The anharmonic oscillator (AHO) results were plotted for all temperatures, but the full data for each E_v(T) model is included in Table VII in Appendix B. The data are compared to the same models, with the addition of the Macheret–Fridman model and the Park two-temperature correction, again calculated at the measured T_v and simulated T_{tr}. As expected from the ε results, the best-fit from Table I reproduces the data trend and the results only deviate slightly from the MMT model values for O_2–O_2 collisions with non-Boltzmann correction.

None of the CVDV models perfectly captures the behavior of the experimental data, but the MMT model with a non-Boltzmann correction results in close agreement.[1] As stated for the ε results, the MMT model uses the REAQCT model for E_v(T); thus, a fair comparison requires the experimental results interpreted using the REAQCT model (Table VII). However, once again the MMT model with non-Boltzmann correction falls within the uncertainty bounds of nearly all

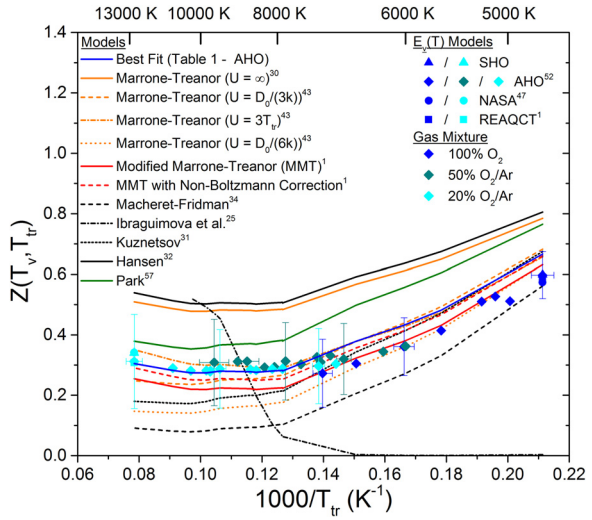

FIG. 10. Vibrational coupling factor (Z) as a function of translational/rotational temperature (T_{tr}). Each data point has a corresponding vibrational temperature (T_v) specified in Appendix B. The highest and lowest temperature conditions show Z calculated using four models for $E_v(T)$.[1,47,52] Although the results are compared to multiple models, the experimental results trend most similarly to the MMT model with non-Boltzmann correction and overlap with the Park two-temperature model at high temperatures.[1,25,30–32,34,43,57]

experimental data regardless of $E_v(T)$ model. This is partially because the uncertainty for Z was amplified through the vibrational partition functions, Q(T), in the Marrone and Treanor theory calculation [Eqs. (4) and (5)]. Of the considered CVDV models, only the MMT model reproduces the experimental behavior over the full temperature range.

The Park model, though not a full CVDV model, provides a recommendation to account for the slowing of dissociation due to vibrational nonequilibrium.[56] Instead of using Z, the Park model suggests using the geometric mean of T_v and T_{tr} as a pseudotemperature to account for the effect of vibrational equilibrium on dissociation. However, the Park correction can be expressed in the same form as the other CVDV models by dividing the two-temperature dissociation rate constant [$k_d(\sqrt{T_v T_{tr}})$] by the one-temperature dissociation rate constant [$k_d(T_{tr})$] [Eq. (21)],

$$Z_{Park} = \frac{k_d\left(\sqrt{T_v T_{tr}}\right)}{k_d(T_{tr})}. \tag{21}$$

Figure 10 plots this ratio using the Park recommendation for the O_2–O_2 dissociation rate constant, the measured T_v, and the simulated T_{tr}. The Park model results trend similarly to the experimental data and agree somewhat at high temperatures, though this agreement breaks down at lower temperatures. However, the Park model does not include a mechanism for vibrational energy loss through dissociation (i.e., ε), so the full Park two-temperature model does not predict the persistent suppression of T_v below T_{tr} for the O_2–Ar results. While the Park model provides reasonable agreement with the experimental data, the model framework lacks the vibrational energy loss mechanism that was critical to isolating Z from experimental time-histories.

Of the remaining models, the Hansen model and the Marrone and Treanor model (with $U = \infty$) trend similarly, the Kuznetsov model and the Macheret–Fridman model trend similarly, and the Ibraguimova model trend is significantly different from all the others.[25,30–32,34] As was discussed in Ref. 14, the Hansen model was developed to adapt the Marrone and Treanor model into a form better suited for a fast computational fluid dynamics (CFD) subroutine, thus explaining the similarity. Both the Hansen model and the Marrone and Treanor model (with $U = \infty$) exceed the experimental results, suggesting that high-lying vibrational states exhibit preferential dissociation. As anticipated from the ε results, the empirical values of $U = D_0/(3k)$ and $U = 3T_{tr}$ overlap with the current data, though $U = D_0/(6k)$ differs from the current data at high temperatures.[43] The Kuznetsov model remains within the experimental uncertainty throughout the temperature range, but it predicts smaller values for Z than the current data at high temperature.[31] The Macheret–Fridman model also reproduces the data trend fairly well, though this model generally underpredicts the current data—especially at high temperature.[34] Finally, the Ibraguimova model was developed empirically, which may explain the strongly deviant trend. The Ibraguimova *et al.* experiments were completed in a 4000–10 800 K range, so Fig. 10 only plots the model below 10 800 K. Besides the MMT model, the Kuznetsov model and empirical values for U remain within experimental uncertainty over the full temperature range, but all deviate from the current data to various extents at high temperatures.

4. Dissociation rate constant

Dissociation rate constant results for O_2–O_2 and O_2–O collisions ($k_d^{O_2-O_2}$ and $k_d^{O_2-O}$, respectively), obtained via fits to $n_{O_2}(t)$, extended the measurements to higher temperatures than any previous study (Figs. 11 and 12). Though the $\tau^{O_2-O_2}$ measurements extended to nearly 14 000 K, the k_d measurements only extend to nearly 13 000 K due to the temperature drop throughout the vibrational relaxation process. Overall, the experiments were more sensitive to $k_d^{O_2-O_2}$ than $k_d^{O_2-O}$, resulting in lower uncertainty for $k_d^{O_2-O_2}$. For the 50% O_2–Ar and 20% O_2–Ar experiments, $k_d^{O_2-Ar}$ was calculated using the best-fit expression from Ref. 14 [Eq. (22)]. The current k_d results exhibit consistency across the pure O_2, 50% O_2–Ar, and 20% O_2–Ar data, demonstrate the low scatter of laser absorption measurements, and show reasonable agreement with previous data and models

$$k_{d,BF}^{O_2-Ar} = 3.9 \times 10^{18} T_{tr}^{-1} \exp\left(-59\,380/T_{tr}\right) \mathrm{cm}^3/\mathrm{mol\,s}. \tag{22}$$

a. O_2–O_2 dissociation rate constant. The $k_d^{O_2-O_2}$ results, resolved as a function of T_{tr} for the endothermic dissociation, range from 5000 to 13 000 K and highlight the low scatter and uncertainty of the laser measurements (Fig. 11). As with $\tau^{O_2-O_2}$, the $k_d^{O_2-O_2}$ results, plotted as a function of T_{tr}, also agree within the experimental uncertainty. The data demonstrate the low uncertainty of the measurements, though this uncertainty increased both with higher Ar dilution and in higher temperatures experiments. Finally, the temperature-resolved results demonstrate the good agreement of the data to the current best-fit expression [Eq. (23)],

$$k_{d,BF}^{O_2-O_2} = 9.5 \times 10^{21} T_{tr}^{-1.7} \exp\left(-59\,400/T_{tr}\right) \mathrm{cm}^3/\mathrm{mol\,s}. \tag{23}$$

The current best-fit Arrhenius equation for $k_d^{O_2-O_2}$ shares some similarities with the included models [Eq. (23)]. The current best-fit

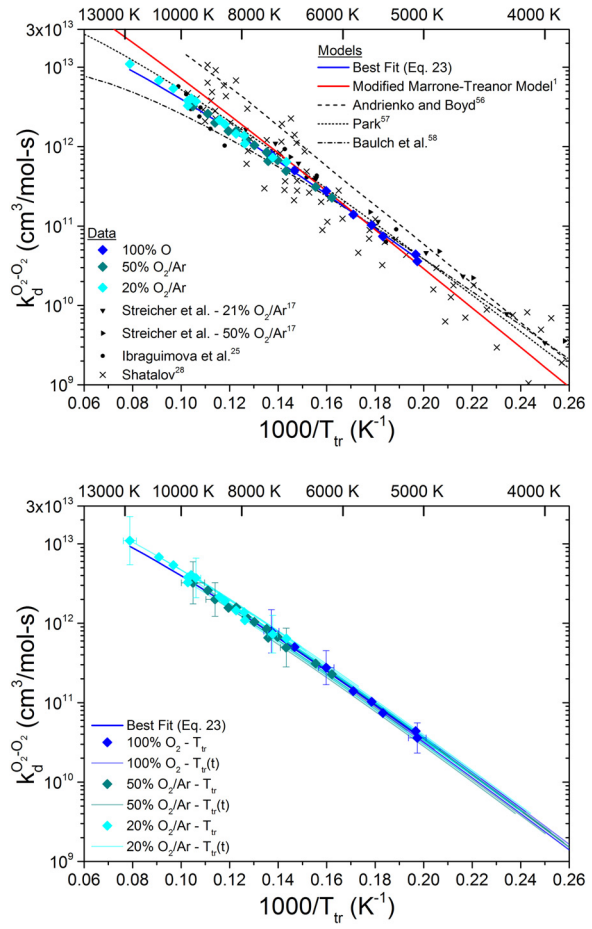

FIG. 11. Arrhenius plots depicting $k_d^{O_2-O_2}$ as a function of T_{tr}. The first plot provides a comparison of the current data to literature data and models.[1,17,25,28,43,56,57] The data points were sampled from the portion of the time-history with the highest sensitivity to $k_d^{O_2-O_2}$, and the lines in the second plot denote the evolution of $k_d^{O_2-O_2}$ as T_{tr} decreased. For the 50% O_2–Ar and 20% O_2–Ar experiments, $k_d^{O_2-Ar}$ was taken from prior work to isolate $k_d^{O_2-O_2}$.[14]

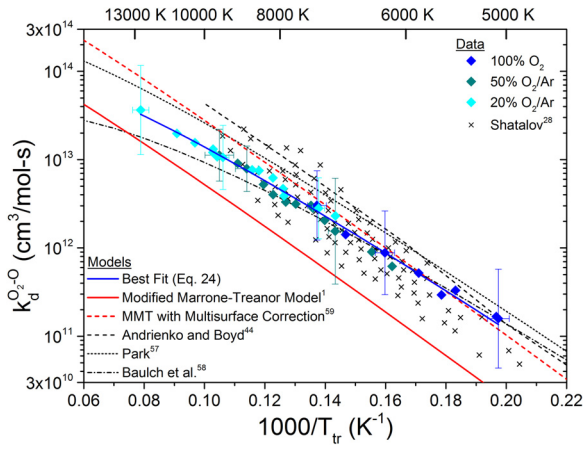

FIG. 12. Arrhenius plot depicting $k_d^{O_2-O}$ as a function of T_{tr} with a comparison of the current data to literature data and models.[1,28,44,56–58] The measurement of $k_d^{O_2-O}$ retained large uncertainties because the time-histories were the least sensitive to $k_d^{O_2-O}$. The data points are plotted for the same temperature conditions as Fig. 11.

found the dissociation temperature (T_d) to be 59 400 K as shown in the exponential term. This value of T_d relates directly to the previously used dissociation energy ($D_0 = 494$ kJ/mol) via the universal gas constant. The Baulch *et al.* model and the Park model both found similar values for T_d (59 380 and 59 500 K, respectively), but the MMT model specifies a slightly larger T_d (60 540 K) that was fit from the QCT data and partially accounts for the steeper slope of this model. The Andrienko and Boyd model does not express the model results in an Arrhenius form, but the slope suggests it too would return a larger T_d than the current best-fit equation. The current best-fit found a pre-exponential temperature exponent of −1.7, and this value falls between the values of the Baulch *et al.* model and the Park model (−2.5 and −1.5, respectively). The temperature exponent accounts for the divergence of the Baulch *et al.* model and the Park model at high temperatures. Again, the MMT model value of −0.77 differs from aforementioned values, and this also contributes to the steeper slope of the MMT model. Overall, both T_d and the temperature exponent account for the slightly different slopes of each model, whereas the temperature exponent mostly accounts for the divergence among the models at high temperatures.

None of the models quite reproduce the current $k_d^{O_2-O_2}$ data, especially at high temperatures, but the Park model best reproduces the data trend (Fig. 11). The Andrienko and Boyd model exceeds the current data and the other models by roughly a factor of two for the temperature range of this study. The Baulch *et al.* model, the Park model, and the MMT model all reasonably reproduce the data below 8000 K, but these three models diverge at higher temperatures. The Baulch *et al.* model underpredicts the experimental data, but both the Park model and the MMT model mostly remain within the experimental uncertainty. Of the two, the Park model best reproduces the experimental data, although the MMT model provides an acceptable prediction of $k_d^{O_2-O_2}$.

Finally, the current data exhibit much lower scatter than any of the previous studies, again highlighting the advantages of UV laser absorption diagnostics for isolating CVDV rate parameters (Fig. 11). All of the data from previous works were obtained using the absorption of UV light, but most of the previous studies used broadband light sources dispersed via monochromators.[25,28] The much wider spectrum from the broadband light sources reduced the vibrational-state specificity of the measurements and noise from the monochromators and photomultipliers contributed to the large scatter in the previous studies. In contrast, the narrow spectrum of the UV laser light and simpler detection optics resulted in low scatter and uncertainty for the current work. Of the previous studies, the work by Ibraguimova *et al.* exhibits the lowest scatter, and their study overlaps with the current results. This work improved upon the Ibraguimova *et al.* results by extending measurements to higher temperatures and reducing the uncertainty with the UV laser absorption diagnostics. Unlike the prior studies, the current work results in the low scatter and uncertainty necessary to distinguish between models.

b. O_2–O dissociation rate constant. The $k_d^{O_2-O}$ results, plotted for the same temperatures as $k_d^{O_2-O_2}$, also exhibit low scatter, but these measurements exhibit much higher uncertainty due to the lower sensitivity of the reaction to $k_d^{O_2-O}$ (Fig. 12). Due to the increased uncertainty, $k_d^{O_2-O}$ was not resolved as a function of T_{tr} for the endothermic dissociation. The uncertainty was generally larger because of the lower sensitivity to $k_d^{O_2-O}$ (Fig. 7). However, the uncertainty was also larger for lower temperatures and higher Ar dilution because those experiments produced fewer O atoms. Ultimately, $k_d^{O_2-O}$ data were best fit with a very similar expression as $k_d^{O_2-O_2}$ but increased by a constant factor of 3.5 [Eq. (24)]

$$k_{d,BF}^{O_2-O} = 3.3 \times 10^{22} T_{tr}^{-1.7} \exp\left(-59\,400/T_{tr}\right) \mathrm{cm}^3/\mathrm{mol\,s}. \quad (24)$$

The $k_d^{O_2-O}$ best-fit Arrhenius equation shares similarities with the Baulch *et al.* model, the Park model, and the Andrienko and Boyd model, but the MMT model significantly underpredicts the current results [Eq. (24)]. All of the considered models used the same T_d and temperature exponent values as their $k_d^{O_2-O_2}$ expressions with the exception of the MMT model. The MMT model used a T_d of 60 552 K and a temperature exponent of −0.65, which are similar to the O_2–O_2 values. Notably, the current best-fit, the Baulch *et al.* model, the Park model and the Andrienko and Boyd model all find values for $k_d^{O_2-O}$ that range from 3 to 5 times larger than the $k_d^{O_2-O_2}$ fits. On the other hand, $k_d^{O_2-O}$ and $k_d^{O_2-O_2}$ for the MMT model essentially overlap. The current best-fit supports the use of a larger $k_d^{O_2-O}$ than the MMT model.

Other quasi-classical trajectory (QCT) results have likewise found discrepancy between modeled and experimental O_2–O rates, so many past QCT results apply a multisurface correction factor of 16/3 to better align the models and experiments.[58–60] This multisurface correction factor accounts for the role of multiple electronic configurations of the three-atom system for O_2–O collisions. In particular, the O_3 system exhibits spin and spatial symmetries between ground-state, triplet O_2 and ground-state, triplet O. These symmetries result in nine adiabatic electronic states for the O_3 system: three singlet states, three triplet states, and three quintet states.[41] The O_4 system does not exhibit these symmetries, so a multisurface correction was not relevant to the earlier O_2–O_2 dissociation rate constant results. Full discussion of the O_3 potential energy surfaces can be found in Ref. 41, while the multisurface correction factor is discussed in Refs. 58–60. As expected, the 16/3 correction factor results in better agreement between the MMT model results and the current experiments, and the corrected results fall entirely within the bounds of experimental uncertainty.

The larger uncertainty of the $k_d^{O_2-O}$ data hinders the comparison of the current data to the models. Again, none of the models reproduce the current $k_d^{O_2-O}$ data, especially at high temperatures, but the Andrienko and Boyd model, the Baulch *et al.* model, the Park model, and corrected MMT model all remain within the experimental uncertainty (Fig. 12). The Andrienko and Boyd model again exceeds the current data and the other models by roughly a factor of two, but the experimental uncertainty spans a similar range. The Park model exceeds the $k_d^{O_2-O}$ data more than it exceeded the $k_d^{O_2-O_2}$ data, whereas the Baulch *et al.* model behaves similarly for both $k_d^{O_2-O}$ and $k_d^{O_2-O_2}$. The large uncertainty obscures the comparison between the Andrienko and Boyd model, the Baulch *et al.* model, the Park model, and the MMT model with multisurface correction.

The current data again exhibit much lower scatter than a previous study that used broadband UV light and monochromators (Fig. 12).[28] The other studies that measured $k_d^{O_2-O_2}$ did not purport to measure $k_d^{O_2-O}$, opting instead to either neglect O_2–O dissociation or assume a constant ratio of $k_d^{O_2-O}$ to $k_d^{O_2-O_2}$. For example, the Ibraguimova *et al.* study assumed that $k_d^{O_2-O}$ was 3.5 times larger than $k_d^{O_2-O_2}$, the same as was found in the current study. While the current $k_d^{O_2-O}$ data exhibit much lower scatter than the Shatalov study, the current experimental uncertainty still spans the scatter in the Shatalov data. This study was able to isolate $k_d^{O_2-O}$ with low scatter, but the sensitivity to O_2–O collisions was small, resulting in large uncertainty. Overall, the $k_d^{O_2-O}$ results highlight the unique capabilities of UV laser absorption diagnostics for isolating multiple reaction rate coefficients from a single shock-tube experiment.

IV. CONCLUSIONS

The experimental setup used in this work produced well-defined and controlled high-temperature and low-pressure conditions, and the two UV laser absorption diagnostics provided an *in situ*, quantum-state-specific method to probe vibrational state populations (Fig. 1).[14,17,18] This combination of tightly controlled conditions and sensitive diagnostics resulted in the high-quality absorbance time-histories at 223.237 nm and 236.9 nm, which correspond to $v'' = 5$ and 6, respectively (Figs. 3, 13, and 14).[19,20] These absorbance time-histories improved upon previous work by increasing the signal-to-noise ratio and by adding continuous-wave laser light to increase the vibrational state sensitivity. As in previous work, the absorbance ratio was used to calculate T_v, the magnitude of absorbance at either wavelength was used to calculate n_{O_2}, and a Boltzmann distribution using n_{O_2} and T_v was used to calculate $n_{v''}$. The temperature time-histories demonstrated the ability to distinguish the depression of T_v below T_{tr} throughout the experimental test time for O_2–Ar experiments (Figs. 5 and 16). Meanwhile, the pure O_2 experiments exhibited a convergence between T_v and T_{tr}—likely due to the fast O_2–O relaxation (Fig. 15). The $n_{v''}$ time-histories demonstrated the quantum-state specificity of this work, whereas the n_{O_2} time-histories showcased the competing effects of density increase and dissociation (Figs. 6, 17, and 18). In this work, the uncertainty of the T_v, n_{O_2}, and $n_{v''}$ time-histories was significantly reduced because of the improved absorbance signals and more sensitive UV laser diagnostics. These low-uncertainty T_v, n_{O_2}, and $n_{v''}$ time-histories were central to the isolation of the CVDV model parameters [Eqs. (1) and (2)].

Unlike the dilute O_2–Ar study, the higher oxygen concentrations utilized in this work resulted in larger decreases in T_{tr} due to the endothermic vibrational relaxation and dissociation processes, so the analysis used energy conservation to calculate the decreases in T_{tr} and used mass conservation to determine the magnitude of the gas motion (Fig. 2). Ultimately, the gas motion was used to account for slight differences between the lab time—in which the time-histories were measured—and the particle time—from which the CVDV rate parameters were inferred. The magnitude of this correction was kept small by making measurements 5 mm from the end wall, and overall this effect exhibited a timing difference of less than 5 μs even in the highest temperature cases. To illustrate the effect of particle motion, the best-fit absorbance simulations were plotted against both lab time and particle time (Figs. 3, 13, and 14). Accounting for the effects of density

change and test gas motion was integral to obtaining accurate results for the inferred CVDV rate parameters.

The time-history results provide several options for comparisons to computational models. Zero-dimensional model results can be compared to the particle-time-adjusted measured time-histories to infer CVDV rate parameters, whereas models that include the one-dimensional incident and reflected shock processes can be compared to the lab-time measurements at 5 mm from the end wall.[61] The experimental conditions included in Tables II–IV in Appendix B provide additional information about the fill pressure, non-ideal pressure rise, shock velocity, and shock attenuation to assist with model comparisons. The low uncertainty and high time resolution of this work provide appropriate test cases for computational model validation.

The CVDV rate parameter results demonstrate the sensitivity of laser absorption diagnostics for inferring vibrational energy excitation and dissociation rates to higher temperatures than had been previously achieved.[14] Each of the five inferred CVDV rate parameters ($\tau^{O_2-O_2}$, ε, Z, $k_d^{O_2-O_2}$, and $k_d^{O_2-O}$) exhibits reasonably low scatter and uncertainty among the pure O_2, 50% O_2–Ar, and 20% O_2–Ar experiments and was compared to relevant models and previous data (Figs. 8–12). The results for $\tau^{O_2-O_2}$ were resolved as a function of T_{tr} throughout the endothermic vibrational relaxation process, and the data show a reduced temperature dependence at high temperatures than previous data and models (Fig. 8). The clustering in the ε results based on mixture composition implies that each collision partner—Ar, O_2, and O—may require a separate ε, but the current diagnostics did not resolve this difference (Figs. 9 and 10). However, this clustering was not apparent in the Z results. Additionally, both the ε and Z results demonstrate a reasonably good fit of the same form as the MMT model, but the values deviate slightly from the MMT model predictions (Table I).[1] Finally, the $k_d^{O_2-O_2}$ and $k_d^{O_2-O}$ results highlight the much lower scatter than previous measurements, with $k_d^{O_2-O_2}$ resolved as a function of T_{tr} throughout the endothermic dissociation process (Figs. 11 and 12).

Many of the models only provided recommendations for one or two of the CVDV rate parameters, but the Andrienko and Boyd models, Ibraguimova *et al.* experiments, Park two-temperature model, and MMT model all recommended multiple CVDV rate parameters.[1,25,43,44,55,56]

The Andrienko and Boyd models generally differ from the current data significantly, though they reproduce the data trends reasonably well.[43,44] For $\tau^{O_2-O_2}$, the Andrienko and Boyd models underpredict the experimental results by about a factor of two, but they exceed the experimental results by a factor of two for $k_d^{O_2-O_2}$ and $k_d^{O_2-O}$.

The Ibraguimova data for $\tau^{O_2-O_2}$ and $k_d^{O_2-O_2}$ exhibit reasonably consistency with the current results, but the current results demonstrate a larger reduction in the temperature dependence of $\tau^{O_2-O_2}$.[25] Additionally, the Ibraguimova *et al.* assumption that $k_d^{O_2-O}$ was 3.5 times larger than $k_d^{O_2-O_2}$ is supported by the current experimental results. However, the empirical fits for ε and Z vastly differ both in trend and magnitude from the current results and previous models.

The Park two-temperature model provides recommendations for $k_d^{O_2-O_2}$ and $k_d^{O_2-O}$ as well as a correction to account for the effect of vibrational nonequilibrium on dissociation.[56] The three parameters affecting dissociation ($k_d^{O_2-O_2}$, $k_d^{O_2-O}$, and Z) show relatively good agreement with the current experiments. However, the parameters in the Park model affecting vibrational energy transfer ($\tau^{O_2-O_2}$) and loss (ε) exhibit poor agreement with experiments. Park provided two recommendations for $\tau^{O_2-O_2}$—one based on thermochemical relaxation in shock tunnels and one based on the collision time correction, and

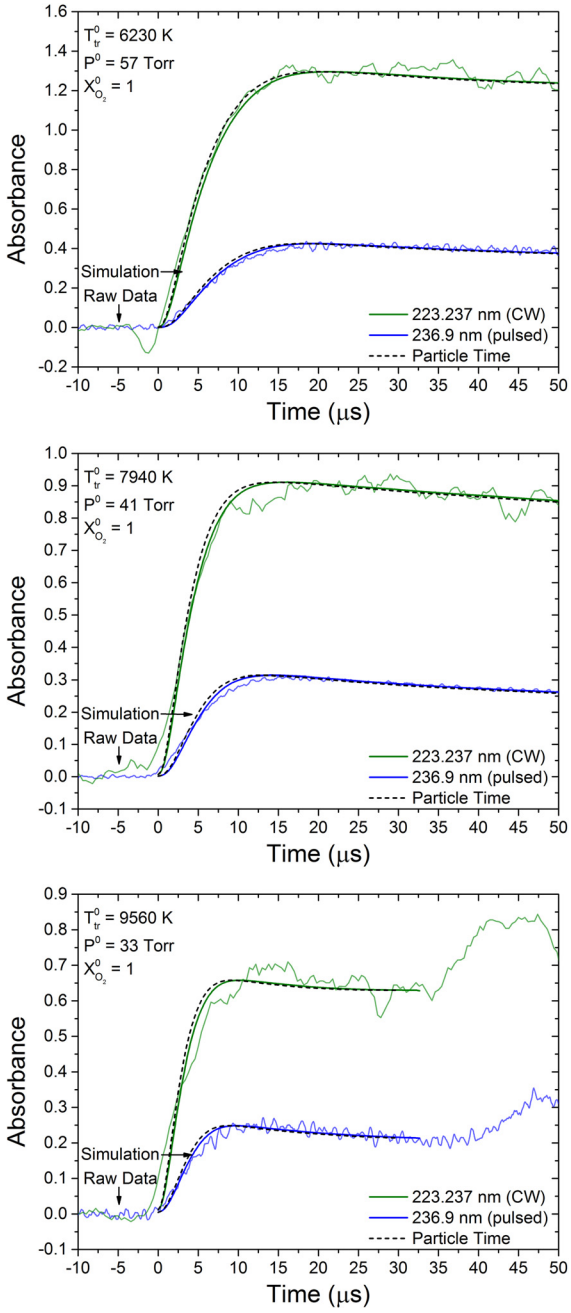

FIG. 13. Absorbance (α) time-histories for coupled vibration-dissociation shocks using pure O_2 at three temperature conditions. The raw data demonstrate low noise of the laser diagnostics, the best-fit simulations show good agreement with the raw data, and the particle-time simulations illustrate the effect of density change. The wavelengths were selected to probe $v'' = 5$ and 6, respectively.

neither recommendation fully agrees with the experimental data (Fig. 8).[55,56] However, due to the lack of inclusion of ε, the Park model would predict the convergence of T_v and T_{tr} in all cases instead of the observed suppression of T_v below T_{tr} for the O_2–Ar mixtures. While the dissociation parameters of the Park model reasonably agree with experimental data, the Park model framework cannot reproduce the observed behavior of the temperature time-histories.

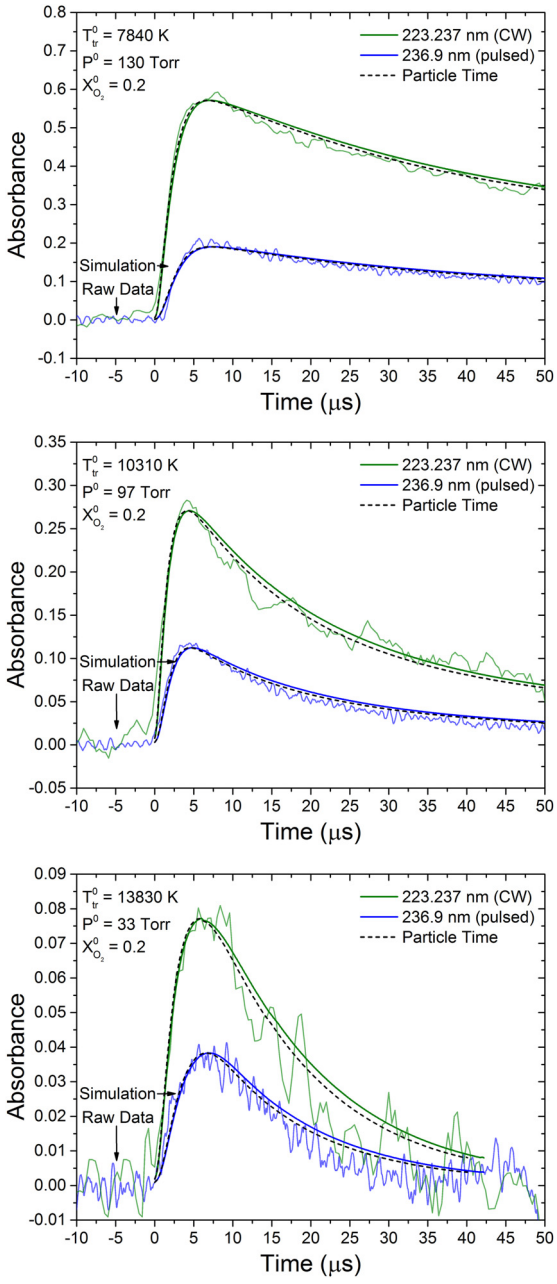

FIG. 14. Absorbance (α) time-histories for coupled vibration-dissociation shocks using 20% O_2 in Ar at three temperature conditions. The best-fit simulations show good agreement with the raw data, and the particle-time simulations illustrate the effect of density change. The noise in the highest temperature case was more pronounced due to the low absorbance at low pressures. The wavelengths were selected to probe $v'' = 5$ and 6, respectively.

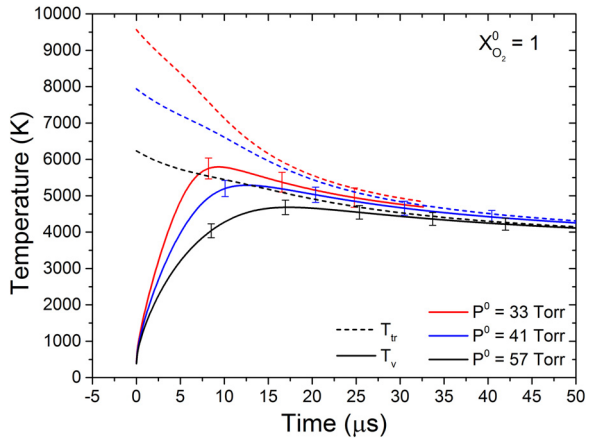

FIG. 15. Vibrational temperature (T_v) time-histories for three pure O_2 experiments that demonstrate diagnostic sensitivity. While O_2–Ar mixtures exhibited a suppression of T_v below T_{tr}, the pure O_2 time-histories converge likely due to the role of fast vibrational relaxation via O_2–O collisions. The translational/rotational temperature (T_{tr}) time-histories were simulated using energy conservation and enthalpy values from literature [Eq. (12)].[47]

Finally, the MMT model provides recommendations for all of the five CVDV rate parameters.[1] The MMT model provided good agreement with the current data for ε and Z, particularly with the non-Boltzmann correction. Similarly, the $k_d^{O_2-O_2}$ prediction of the MMT model falls within the uncertainty of the current experimental results. Conversely, the $k_d^{O_2-O}$ prediction of the MMT model significantly underpredicts the current experimental results, even with the increased experimental uncertainty. However, the multisurface correction factor of 16/3 recommended by many previous QCT models results in much

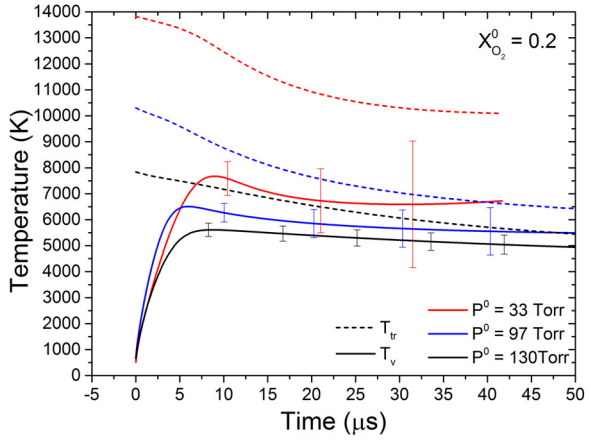

FIG. 16. Vibrational temperature (T_v) time-histories for three 20% O_2 in Ar experiments that demonstrate diagnostic sensitivity and the suppression of T_v below T_{tr}. The translational/rotational temperature (T_{tr}) time-histories were simulated using energy conservation and enthalpy values from literature [Eq. (12)].[47]

better agreement between the MMT model and experimental data for $k_d^{O_2-O}$. Finally, the use of the Millikan and White correlation with a collision-time correction (as suggested by Park) again significantly underpredicts the current $\tau^{O_2-O_2}$ results. The good agreement for ε and Z with worse agreement for $k_d^{O_2-O_2}$, $k_d^{O_2-O}$, and $\tau^{O_2-O_2}$ suggests that the MMT model reasonably describes the distribution of the vibrational states of dissociating molecules but does not fully predict the magnitude of the vibrational excitation and dissociation rates.

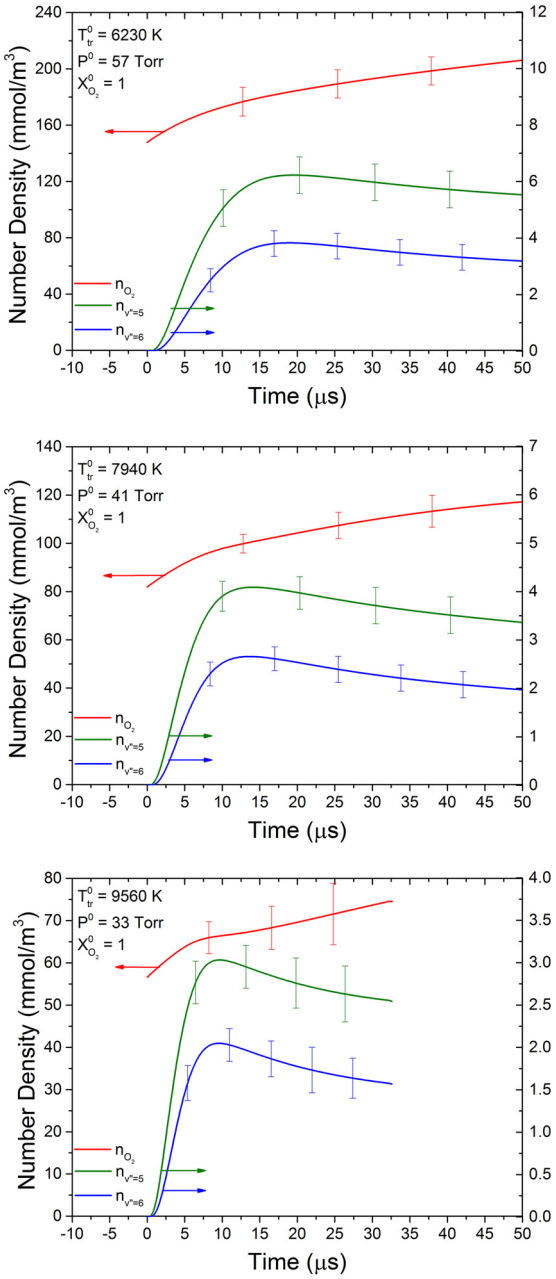

FIG. 17. Number density time-histories for the total amount of O_2 (n_{O_2}) and for specific vibrational levels ($n_{v''}$) measured in three pure O_2 experiments. In this case, n_{O_2} increases due to the strong decrease in T_{tr}, which corresponded to an increased gas density. The $n_{v''}$ behavior more closely follows α because the wavelengths were selected to probe $v'' = 5$ and 6, respectively. Overall, these results demonstrate low uncertainty and quantum-state specificity.

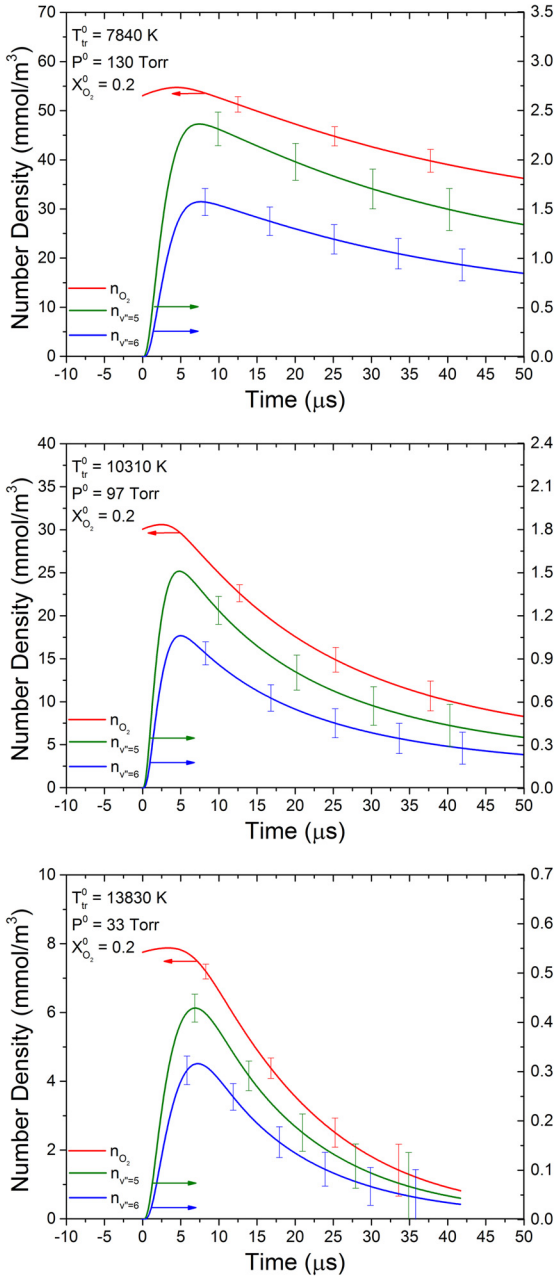

FIG. 18. Number density time-histories for the total amount of O_2 (n_{O_2}) and for specific vibrational levels ($n_{v''}$) measured in three 20% O_2 in Ar experiments. In this case, n_{O_2} decreases due to the smaller decrease in T_{tr} and nearly complete dissociation. The $n_{v''}$ behavior more closely follows α because the wavelengths were selected to probe $v'' = 5$ and 6, respectively. Overall, these results demonstrate low uncertainty and quantum-state specificity.

TABLE II. 100% O_2 initial condition summary. Boldface denotes the plotted absorbance, temperature, and state-specific number density time-histories (Figs. 13, 15, and 17).

Ref.	T_{tr}^0 (K)	P^0 (Torr)	P_{fill} (Torr)	dP/dt (Torr/μs)	U_{is} (mm/μs)	U_{rs} (mm/μs)	Atten. (%/m)
100-1	6230	57	0.13	0.10	2.22	0.77	0.62
100-2	6300	89	0.19	0.13	2.23	0.76	0.73
100-3	6800	63	0.13	0.12	2.32	0.80	0.51
100-4	6890	37	0.08	0.19	2.34	0.81	0.05
100-5	7340	30	0.05	0.24	2.41	0.83	0.93
100-6	7940	41	0.07	0.15	2.51	0.87	−0.91
100-7	8750	26	0.04	0.42	2.64	0.91	−1.39
100-8	9560	34	0.05	0.24	2.76	0.95	−0.33

TABLE III. 50% O_2–Ar initial condition summary. Boldface denotes the plotted absorbance, pressure, temperature, and state-specific number density time-histories (Figs. 3–6).

Ref.	T_{tr}^0 (K)	P^0 (Torr)	P_{fill} (Torr)	dP/dt (Torr/μs)	U_{is} (mm/μs)	U_{rs} (mm/μs)	Atten. (%/m)
50-01	7100	122	0.36	0.13	2.07	0.86	0.82
50-02	7430	100	0.26	0.13	2.12	0.88	0.91
50-03	8110	75	0.18	0.12	2.21	0.91	0.06
50-04	8410	125	0.30	0.20	2.25	0.93	0.31
50-05	8580	60	0.14	0.12	2.28	0.94	0.47
50-06	8720	110	0.24	0.18	2.30	0.95	0.18
50-07	8980	49	0.11	0.13	2.33	0.96	0.37
50-08	9370	77	0.16	0.19	2.38	0.98	0.20
50-09	9530	39	0.08	0.15	2.40	0.99	0.29
50-10	9820	35	0.06	0.14	2.44	1.00	0.52
50-11	10470	53	0.10	0.30	2.52	1.03	−0.46
50-12	10910	58	0.12	0.20	2.58	1.05	−1.54
50-13	11410	30	0.06	0.36	2.63	1.08	0.67

TABLE IV. 20% O_2–Ar initial condition summary. Boldface denotes the plotted absorbance, temperature, and state-specific number density time-histories (Figs. 14, 16, and 18).

Ref.	T_{tr}^0 (K)	P^0 (Torr)	P_{fill} (Torr)	dP/dt (Torr/μs)	U_{is} (mm/μs)	U_{rs} (mm/μs)	Atten. (%/m)
20-01	7530	160	0.60	0.11	1.96	0.92	0.42
20-02	7840	130	0.47	0.09	2.00	0.94	0.72
20-03	8570	91	0.29	0.11	2.09	0.98	0.64
20-04	8580	208	0.70	0.26	2.09	0.98	0.77
20-05	8810	186	0.61	0.22	2.12	0.99	0.42
20-06	9190	68	0.19	0.12	2.17	1.01	0.73
20-07	9380	148	0.43	0.24	2.19	1.02	0.47
20-08	10310	97	0.25	0.23	2.30	1.07	0.40
20-09	10410	42	0.10	0.09	2.31	1.07	0.80
20-10	10600	42	0.10	0.14	2.33	1.08	−0.10
20-11	10620	83	0.20	0.23	2.33	1.08	0.27
20-12	11270	64	0.15	0.23	2.40	1.12	0.62
20-13	12030	51	0.10	0.21	2.48	1.15	0.56
20-14	13830	33	0.06	0.29	2.67	1.23	−0.29

TABLE V. Vibrational relaxation time (τ) data.

Ref.	T_{tr} (K)	$T_{tr}^{-1/3}$ ($K^{-1/3}$)	$P\tau$ (atm-μs)
100-1	5990	0.0551	0.420
100-2	6040	0.0549	0.405
100-3	6590	0.0534	0.331
100-4	6670	0.0531	0.350
100-5	7090	0.0520	0.348
100-6	7730	0.0506	0.308
100-7	8470	0.0491	0.289
100-8	9280	0.0476	0.264
50-01	6960	0.0524	0.357
50-02	7290	0.0516	0.334
50-03	7980	0.0501	0.335
50-04	8280	0.0494	0.312
50-05	8440	0.0491	0.287
50-06	8590	0.0488	0.283
50-07	8850	0.0484	0.273
50-08	9210	0.0477	0.274
50-09	9380	0.0474	0.276
50-10	9670	0.0469	0.261
50-11	10340	0.0459	0.230
50-12	10760	0.0453	0.231
50-13	11260	0.0446	0.215
20-01	7460	0.0512	0.313
20-02	7770	0.0505	0.292
20-03	8500	0.0490	0.277
20-04	8530	0.0490	0.253
20-05	8770	0.0485	0.265
20-06	9120	0.0479	0.263
20-07	9340	0.0475	0.266
20-08	10240	0.0460	0.212
20-09	10340	0.0459	0.215
20-10	10530	0.0456	0.219
20-11	10550	0.0456	0.232
20-12	11200	0.0447	0.209
20-13	11970	0.0437	0.201
20-14	13770	0.0417	0.180

TABLE VI. O_2–O_2 ($k_d^{O_2-O_2}$) and O_2–O ($k_d^{O_2-O}$) dissociation rate constant data.

Ref.	T_{tr} (K)	$1000/T_{tr}$ (K^{-1})	$k_d^{O_2-O_2}$ (cm^3/mol s)	$k_d^{O_2-O}$ (cm^3/mol s)
100-1	5070	0.197	3.60×10^{10}	1.59×10^{11}
100-2	5080	0.197	4.39×10^{10}	1.67×10^{11}
100-3	5460	0.183	7.41×10^{10}	3.31×10^{11}
100-4	5600	0.179	1.03×10^{11}	2.95×10^{11}
100-5	5850	0.171	1.39×10^{11}	5.20×10^{11}
100-6	6260	0.160	2.76×10^{11}	8.80×10^{12}
100-7	6810	0.147	5.03×10^{11}	1.42×10^{12}
100-8	7290	0.137	7.92×10^{11}	3.03×10^{12}
50-01	6170	0.162	2.28×10^{11}	6.20×10^{11}
50-02	6430	0.155	3.11×10^{11}	9.04×10^{11}
50-03	6980	0.143	4.94×10^{11}	1.55×10^{12}
50-04	7150	0.140	6.74×10^{11}	2.06×10^{12}
50-05	7360	0.136	6.56×10^{11}	2.82×10^{12}
50-06	7390	0.135	8.48×10^{11}	3.02×10^{12}
50-07	7680	0.130	1.04×10^{12}	3.15×10^{12}
50-08	7880	0.127	1.20×10^{12}	3.32×10^{12}
50-09	8150	0.123	1.58×10^{12}	4.01×10^{12}
50-10	8360	0.120	1.57×10^{12}	5.23×10^{12}
50-11	8770	0.114	2.00×10^{12}	7.89×10^{12}
50-12	9010	0.111	2.60×10^{12}	9.05×10^{12}
50-13	9530	0.105	3.23×10^{12}	1.12×10^{13}
20-01	6980	0.143	6.43×10^{11}	2.31×10^{12}
20-02	7260	0.138	7.28×10^{11}	2.82×10^{12}
20-03	7920	0.126	1.09×10^{12}	3.89×10^{12}
20-04	7940	0.126	1.38×10^{12}	4.70×10^{12}
20-05	8150	0.123	1.45×10^{12}	6.22×10^{12}
20-06	8470	0.118	1.91×10^{12}	7.52×10^{12}
20-07	8630	0.116	2.16×10^{12}	7.67×10^{12}
20-08	9420	0.106	3.72×10^{12}	1.06×10^{13}
20-09	9600	0.104	4.06×10^{12}	1.08×10^{13}
20-10	9720	0.103	3.79×10^{12}	1.31×10^{13}
20-11	9730	0.103	3.27×10^{12}	1.21×10^{13}
20-12	10330	0.097	5.38×10^{12}	1.55×10^{13}
20-13	11000	0.091	6.82×10^{12}	1.98×10^{13}
20-14	12680	0.079	1.10×10^{13}	3.65×10^{13}

Of all of the model comparisons, the MMT model provides the most comprehensive and accurate comparison to the current experimental data.

Future work can leverage the methods and results of this study to isolate more high-temperature internal energy excitation and chemical reaction rates relevant to air. Continued studies of high-temperature O_2 would benefit from the investigation of the low-lying excited electronic states ($a^1\Delta_g$ and $b^1\Sigma_g^+$), because the electronic excitation process critically lacks kinetic data. Additionally, some models predict that these electronic states play a significant role in speeding the dissociation of O_2 in hypersonic flows, so the development of laser diagnostics to probe these states provides an opportunity for unique model validation data.[62] The current results for O_2–O_2 rates can be leveraged in futures studies, especially those that include N_2. The O_2 reactions probed in this study represent an important subset of the reactions that influence high-temperature air, but N_2 reactions—especially those that involve NO—provide a clear target for similar shock tube studies.[8–10] The current quantum-state specific laser diagnostics used in this work remain applicable to a range of nonequilibrium phenomena in high-temperature air, and expanding upon the current diagnostics, methods, and results can similarly probe many more important nonequilibrium phenomena for high-temperature air.

ACKNOWLEDGMENTS

The authors would like to thank Dr. David F. Davidson and Dr. Christopher L. Strand in the mechanical engineering department at Stanford University for their assistance with troubleshooting shock tube and laser diagnostic issues. The authors would also like to thank Professor Kyle M. Hanquist in the aerospace and mechanical engineering department at the University of Arizona, Dr. Ross S. Chaudhry and Professor Iain D. Boyd in the aerospace engineering sciences department at the University of Colorado Boulder, and Professor Sergey F. Gimelshein in the astronautical engineering department at the University of Southern California for discussions about computational modeling. This work was supported by the Air Force Office of Scientific Research through AFOSR Grant No. FA9550-16-1-0291 with contract monitors Dr. I. Leyva and Dr. S. Popkin.

APPENDIX A: ADDITIONAL TIME-HISTORY RESULTS FOR PURE O_2 AND 20% O_2–AR

The following figures contain additional time-history results for three pure O_2 experiments (Figs. 13, 15, and 17) and three 20% O_2 in Ar experiments (Figs. 14, 16, and 18). Figures 13 and 14 provide additional absorbance time-histories that show the raw data, best-fit simulation, and particle-time simulation. Together, these

TABLE VII. Average vibrational energy loss (ε) and vibrational coupling factor (Z) data.

Ref.	T_{tr} (K)	$1000/T_{tr}$ (K^{-1})	T_v (K)	ε_{SHO}/D_0	ε_{AHO}/D_0	ε_{NASA}/D_0	ε_{REAQCT}/D_0	Z_{SHO}	Z_{AHO}	Z_{NASA}	Z_{REAQCT}
100-1	4730	0.211	4510	0.605	0.640	0.707	0.686	0.599	0.597	0.574	0.581
100-2	4980	0.201	4610	0.586	0.627	0.708	0.682	0.529	0.512	0.479	0.490
100-3	5100	0.196	4760	0.587	0.621	0.687	0.665	0.540	0.527	0.501	0.509
100-4	5220	0.192	4840	0.582	0.615	0.679	0.657	0.524	0.510	0.485	0.494
100-5	5610	0.178	5040	0.559	0.592	0.657	0.634	0.428	0.414	0.387	0.397
100-6	6020	0.166	5260	0.536	0.569	0.629	0.608	0.375	0.361	0.336	0.345
100-7	6640	0.151	5560	0.501	0.534	0.588	0.569	0.319	0.305	0.283	0.290
100-8	7160	0.140	5790	0.471	0.504	0.553	0.536	0.287	0.273	0.253	0.259
50-01	6000	0.167	4970	0.554	0.594	0.667	0.641	0.377	0.362	0.337	0.346
50-02	6270	0.159	5080	0.535	0.573	0.641	0.617	0.359	0.344	0.321	0.329
50-03	6820	0.147	5300	0.498	0.534	0.593	0.572	0.333	0.320	0.301	0.307
50-04	7030	0.142	5440	0.494	0.529	0.582	0.564	0.345	0.331	0.313	0.319
50-05	7190	0.139	5450	0.475	0.510	0.563	0.545	0.323	0.310	0.293	0.298
50-06	7250	0.138	5550	0.482	0.516	0.566	0.549	0.340	0.327	0.309	0.315
50-07	7540	0.133	5560	0.454	0.489	0.536	0.521	0.316	0.302	0.287	0.291
50-08	7830	0.128	5740	0.448	0.482	0.523	0.511	0.326	0.313	0.298	0.302
50-09	8060	0.124	5750	0.424	0.458	0.498	0.487	0.307	0.294	0.280	0.284
50-10	8280	0.121	5810	0.413	0.448	0.484	0.475	0.306	0.292	0.280	0.283
50-11	8680	0.115	6100	0.413	0.448	0.475	0.471	0.327	0.312	0.301	0.303
50-12	8920	0.112	6180	0.404	0.438	0.462	0.460	0.326	0.312	0.302	0.303
50-13	9580	0.104	6390	0.378	0.413	0.425	0.430	0.325	0.309	0.303	0.301
20-01	6940	0.144	5490	0.532	0.565	0.618	0.600	0.318	0.304	0.273	0.280
20-02	7220	0.138	5610	0.515	0.548	0.597	0.581	0.311	0.297	0.268	0.274
20-03	7890	0.127	5890	0.480	0.513	0.552	0.540	0.302	0.287	0.261	0.265
20-04	7890	0.127	5900	0.480	0.513	0.552	0.541	0.304	0.289	0.263	0.267
20-05	8110	0.123	5990	0.470	0.503	0.539	0.529	0.302	0.287	0.262	0.266
20-06	8470	0.118	6120	0.453	0.486	0.516	0.510	0.299	0.283	0.260	0.262
20-07	8600	0.116	6190	0.449	0.482	0.510	0.505	0.302	0.286	0.263	0.265
20-08	9410	0.106	6510	0.420	0.454	0.468	0.472	0.306	0.287	0.271	0.269
20-09	9680	0.103	6540	0.405	0.440	0.450	0.456	0.300	0.281	0.266	0.263
20-10	9700	0.103	6560	0.402	0.437	0.447	0.453	0.297	0.278	0.264	0.261
20-11	9820	0.102	6610	0.401	0.436	0.444	0.451	0.301	0.282	0.268	0.264
20-12	10330	0.097	6760	0.383	0.419	0.417	0.431	0.302	0.282	0.273	0.266
20-13	10990	0.091	7020	0.370	0.407	0.392	0.414	0.312	0.290	0.289	0.276
20-14	12750	0.078	7670	0.342	0.382	0.328	0.373	0.340	0.312	0.341	0.308

plotted values demonstrate the relatively low noise in the raw data and the small effect of density change on the experimental timing. Figures 15 and 16 provide the corresponding temperature time-histories and demonstrate the good sensitivity of the two UV laser diagnostics. Finally, Figs. 17 and 18 show the number density time-histories and highlight the quantum-state specificity of the UV laser measurements. A full description of the experimental conditions for these six experiments can be found in the bold entries of Tables II and IV in Appendix B.

APPENDIX B: TABULATED EXPERIMENTAL CONDITIONS AND CVDV RATE PARAMETERS

The included tables summarize the initial conditions and coupled vibration-dissociation parameters for each experiment included in this study (Tables II–VII). Tables II–IV contain the initial post-reflected-shock temperature (T^0_{tr}), initial post-reflected-shock pressure (P^0), test section fill pressure (P_{fill}) non-ideal pressure rise (dP/dt), incident shock speed (U_{is}), reflected shock speed (U_{rs}), and incident shock attenuation as well as establishing a reference number that is used subsequently. The initial temperature for both the driver and driven sections was the laboratory room temperature of 296 K, and diaphragm burst pressures ranged from 24 to 57 psi. Finally, the diaphragms were located 10 m from the end wall with a driver length of 3.3 m.

The bold reference numbers correspond to the plotted absorbance, pressure, temperature, and state-specific number density time-histories (Figs. 3–6 and 13–18). State-specific number density and vibrational temperature time-histories for each of the other conditions are available by request. Tables V–VII contain the values for translational/rotational temperature (T_{tr}), vibrational temperature, (T_v), and CVDV rate parameters that were inferred from the experimental time-histories. The temperature values in Tables V–VII reflect the plotted values in Figs. 8–12, since the vibrational relaxation time (τ), average vibrational energy loss (ε), vibrational coupling factor (Z), and dissociation rate constants ($k_d^{O_2-O_2}$ and $k_d^{O_2-O}$) were inferred from different portions of the time-histories. Finally, Table VII contains the values for ε and Z inferred using four different models for vibrational energy (E_v).

DATA AVAILABILITY

The data that support the findings of this study are available from the corresponding author upon reasonable request.

REFERENCES

[1]R. S. Chaudhry, I. D. Boyd, E. Torres, T. E. Schwartzentruber, and G. V. Candler, "Implementation of a chemical kinetics model for hypersonic flows in air for high-performance CFD," in Proceedings of AIAA Scitech Forum (2020).

[2]J. Hank, J. Murphy, and R. Mutzman, "The X-51A scramjet engine flight demonstration program," in Proceedings of 15th AIAA International Space Planes and Hypersonic Systems and Technologies Conference, May 2008.

[3]D. Dolvin, "Hypersonic international flight research and experimentation technology development and flight certification strategy," in Proceedings of 16th AIAA/DLR/DGLR International Space Planes and Hypersonic Systems and Technologies Conference (2009).

[4]A. Martin, L. C. Scalabrin, and I. D. Boyd, "High performance modeling of atmospheric re-entry vehicles," J. Phys.: Conf. Ser. **341**, 012002 (2012).

[5]J. Urzay, "Supersonic combustion in air-breathing propulsion systems for hypersonic flight," Annu. Rev. Fluid Mech. **50**, 593–627 (2018).

[6]S. F. Gimelshein and I. J. Wysong, "Validation of high-temperature air reaction and relaxation models using emission data," J. Thermophys. Heat Transfer **33**, 606–616 (2019).

[7]G. V. Candler, "Rate effects in hypersonic flows," Annu. Rev. Fluid Mech. **51**, 379–402 (2019).

[8]D. Bose and G. V. Candler, "Advanced model of nitric oxide formation in hypersonic flows," J. Thermophys. Heat Transfer **12**, 214–222 (1998).

[9]I. D. Boyd, G. V. Candler, and D. A. Levin, "Dissociation modeling in low density hypersonic flows of air," Phys. Fluids **7**, 1757–1763 (1995).

[10]J. P. Monat, R. K. Hanson, and C. H. Kruger, "Shock tube determination of the rate coefficient for the reaction $N_2 + O \rightarrow NO + N$," Symp. (Int.) Combust. **17**, 543–552 (1979).

[11]D. R. White and R. C. Millikan, "Vibrational relaxation of oxygen," J. Chem. Phys. **39**, 1803–1806 (1963).

[12]R. C. Millikan and D. R. White, "Systematics of vibrational relaxation," J. Chem. Phys. **39**, 3209–3213 (1963).

[13]D. R. White, "Shock-tube study of vibrational exchange in N_2–O_2 mixtures," J. Chem. Phys. **49**, 5472–5476 (1968).

[14]J. W. Streicher, A. Krish, R. K. Hanson, K. M. Hanquist, R. S. Chaudhry, and I. D. Boyd, "Shock-tube measurements of coupled vibration-dissociation time-histories and rate parameters in oxygen and argon mixtures from 5000-10 000 K," Phys. Fluids **32**, 076103 (2020).

[15]K. G. Owen, D. F. Davidson, and R. K. Hanson, "Oxygen vibrational relaxation times: Shock tube/laser absorption measurements," J. Thermophys. Heat Transfer **30**, 791–798 (2016).

[16]K. G. Owen, D. F. Davidson, and R. K. Hanson, "Measurements of oxygen dissociation using laser absorption," J. Thermophys. Heat Transfer **30**, 274–278 (2016).

[17]J. W. Streicher, A. Krish, S. Wang, D. F. Davidson, and R. K. Hanson, "Measurements of oxygen vibrational relaxation and dissociation using ultraviolet laser absorption in shock tube experiments," in Proceedings of AIAA Scitech Forum (2019).

[18]J. W. Streicher, A. Krish, and R. K. Hanson, "Vibrational relaxation time measurements in shock-heated oxygen and air from 2000-9000 K using ultraviolet laser absorption," Phys. Fluids **32**, 086101 (2020).

[19]A. Krish, J. W. Streicher, and R. K. Hanson, "Ultraviolet absorbance cross-section measurements of shock-heated O_2 from 2000-8400 K using a tunable laser," J. Quant. Spectrosc. Radiat. Transfer **247**, 106959 (2020).

[20]A. Krish, J. W. Streicher, and R. K. Hanson, "Spectrally resolved absorption cross-section measurements of shock-heated O_2 for the development of a vibrational temperature diagnostic," J. Quant. Spectrosc. Radiat. Transfer (submitted).

[21]G. Herzberg, *Molecular Spectra and Molecular Structure I. Spectra of Diatomic Molecules*, 2nd ed. (Krieger Publishing Company, Malabar, FL, 1950).

[22]N. G. Bykova and L. A. Kuznetsova, "Study of the absorption characteristics of molecular oxygen in the Schumann-Runge system at high temperatures: I. Calculations of absorption spectra," Opt. Spectrosc. **105**, 668–673 (2008).

[23]N. G. Bykova, I. Zabelinskii, L. B. Ibraguimova, and O. P. Shatalov, "Study of the absorption characteristics of molecular oxygen in the Schumann–Runge system at high temperatures: II. Experiment and comparison with calculation," Opt. Spectrosc. **105**, 674–679 (2008).

[24]M. D. Di Rosa, K. G. Klavuhn, and R. K. Hanson, "LIF spectroscopy of NO and O_2 in high-pressure flames," Combust. Sci. Technol. **118**, 257–283 (1996).

[25]L. B. Ibraguimova, A. L. Sergievskaya, V. Y. Levashov, O. P. Shatalov, Y. V. Tunik, and I. E. Zabelinskii, "Investigation of oxygen dissociation and vibrational relaxation at temperatures 4000–10 800 K," J. Chem. Phys. **139**, 034317 (2013).

[26]S. A. Losev and N. A. Generalov, "A study of the excitation of vibrations and dissociation of oxygen molecules at high temperatures," Sov. Phys. – Dokl. **6**, 1081 (1962).

[27]C. J. Schexnayder, Jr. and J. S. Evans, "Measurements of the dissociation rate of molecular oxygen," NASA Technical Report No. R-108, 1961.

[28]O. P. Shatalov, "Molecular dissociation of oxygen in the absence of vibrational equilibrium," Combust., Explos. Shock Waves **9**, 610–613 (1973).

[29]C. E. Treanor and P. V. Marrone, "Effect of dissociation on the rate of vibrational relaxation," Phys. Fluids **5**, 1022–1026 (1962).

[30]P. V. Marrone and C. E. Treanor, "Chemical relaxation with preferential dissociation from excited vibrational levels," Phys. Fluids **6**, 1215–1221 (1963).
[31]A. Sergievskaya, E. Kovach, S. Losev, and N. Kuznetsov, "Thermal nonequilibrium models for dissociation and chemical exchange reactions at high temperatures," in Proceedings of 31st Thermophysics Conference (1996).
[32]C. F. Hansen, "Vibrational nonequilibrium effects on diatomic dissociation rates," AIAA J. **31**, 2047–2051 (1993).
[33]A. L. Sergievskaya, S. Losev, A. A. Fridman, and S. Macheret, "Selecting two-temperature chemical reaction models for nonequilibrium flows," in Proceedings of 32nd Thermophysics Conference (1997).
[34]H. Luo, A. A. Alexeenko, and S. O. Macheret, "Assessment of classical impulsive models of dissociation in thermochemical nonequilibrium," J. Thermophys. Heat Transfer **32**, 861–868 (2018).
[35]A. Hertzberg, "The application of the shock tube to the study of problems of hypersonic flight," Jet Propul. **26**, 549–568 (1956).
[36]M. F. Campbell, K. G. Owen, D. F. Davidson, and R. K. Hanson, "Dependence of calculated postshock thermodynamic variables on vibrational equilibrium and input uncertainty," J. Thermophys. Heat Transfer **31**, 586–608 (2017).
[37]Z. Hong, K. Y. Lam, D. F. Davidson, and R. K. Hanson, "Broad-linewidth laser absorption measurements of oxygen between 211 and 235 nm at high temperatures," J. Quant. Spectrosc. Radiat. Transfer **112**, 2698–2703 (2011).
[38]P. Hammerling, J. D. Teare, and B. Kivel, "Theory of radiation from luminous shock waves in nitrogen," Phys. Fluids **2**, 422–426 (1959).
[39]H. Bethe and E. Teller, *Deviations from Thermal Equilibrium in Shock Waves* (Aberdeen Proving Ground, MD, 1941).
[40]M. W. Chase, *NIST-JANAF Thermochemical Tables*, 4th ed. (American Institute of Physics for the National Institute of Standards and Technology, 1998), Chap. Oxygen (O).
[41]Z. Varga, Y. Paukku, and D. G. Truhlar, "Potential energy surfaces for $O + O_2$ collisions," J. Chem. Phys. **147**, 154312 (2017).
[42]Y. Paukku, K. R. Yang, Z. Varga, G. Song, J. D. Bender, and D. G. Truhlar, "Potential energy surfaces of quintet and singlet O_4," J. Chem. Phys. **147**, 034301 (2017).
[43]D. A. Andrienko and I. D. Boyd, "High fidelity modeling of thermal relaxation and dissociation of oxygen," Phys. Fluids **27**, 116101 (2015).
[44]D. A. Andrienko and I. D. Boyd, "Rovibrational energy transfer and dissociation in O_2-O collisions," J. Chem. Phys. **144**, 104301 (2016).
[45]J. Hao, J. Wang, and C. Lee, "State-specific simulation of oxygen vibrational excitation and dissociation behind a normal shock," Chem. Phys. Lett. **681**, 69–74 (2017).
[46]R. K. Hanson, "Shock-wave reflexion in a relaxing gas," J. Fluid Mech. **45**, 721–746 (1971).
[47]B. J. McBride, M. J. Zehe, and S. Gordon, "NASA Glenn coefficients for calculating thermodynamic properties of individual species," Technical Report No. NASA TP-2002-211556, September 2002.
[48]C. Park, "The limits of two-temperature kinetic model in air," in Proceedings of 48th AIAA Aerospace Sciences Meeting Including the New Horizons Forum and Aerospace Exposition, January 2010.
[49]J. E. Breen, R. B. Quy, and G. P. Glass, "Vibrational relaxation of O_2 in the presence of atomic oxygen," J. Chem. Phys. **59**, 556 (1973).
[50]J. H. Kiefer and R. W. Lutz, "The effect of oxygen atoms on the vibrational relaxation of oxygen," Symp. (Int.) Combust. **11**, 67–76 (1967).
[51]M. S. Grover, E. Torres, and T. E. Schwartzentruber, "Direct molecular simulation of internal energy relaxation and dissociation in oxygen," Phys. Fluids **31**, 076107 (2019).
[52]Z. Qin, J. M. Zhao, and L. H. Liu, "Radiative transition probabilities for the main diatomic electronic systems of N_2, N_2^+, NO, O_2, CO, CO^+, CN, C_2 and H_2 produced in plasma of atmospheric entry," J. Quant. Spectrosc. Radiat. Transfer **202**, 286–301 (2017).
[53]K. P. Huber and G. H. Herzberg (data prepared by J. W. Gallagher, and R. D. Johnson III), "Constants of diatomic molecules," in *NIST Chemistry WebBook, NIST Standard Reference Database Number 69*, edited by P. J. Linstrom and W. G. Mallard (National Institute of Standards and Technology, Gaithersburg MD, 2018), p. 20899.
[54]J. F. Clarke and M. McChesney, *The Dynamics of Real Gases* (Butterworth, London, 1964), pp. 314–315.
[55]C. Park, "Thermochemical relaxation in shock tunnels," J. Thermophys. Heat Transfer **20**, 689–698 (2006).
[56]C. Park, "Review of chemical-kinetic problems of future NASA missions, I: Earth entries," J. Thermophys. Heat Transfer **7**, 385–398 (1993).
[57]D. L. Baulch, D. D. Drysdale, J. Duxbury, and S. J. Grant, "$O_2 + M \rightarrow O + O + m$," in *Evaluated Kinetic Data for High Temperature Reactions - Homogeneous Gas Phase Reactions of the O2-O3 System, the CO-O2-H2 System, and of Sulphur-Containing Species* (University of Leeds, 1976), Vol. 3, pp. 11–32.
[58]T. K. Mankodi, U. V. Bhandarkar, and B. P. Puranik, "Dissociation cross sections for $N_2 + N \rightarrow 3N$ and $O_2 + O \rightarrow 3O$ using the QCT method," J. Chem. Phys. **146**, 204307 (2017).
[59]R. S. Chaudhry, "Modeling and analysis of chemical kineticsfor hypersonic flows in air," Ph.D. thesis (The University of Minnesota, 2018).
[60]M. S. Grover, T. E. Schwartzentruber, Z. Varga, and D. G. Truhlar, "Vibrational energy transfer and collision-induced dissociation in $O+O_2$ collisions," J. Thermophys. Heat Transfer **33**, 797–807 (2019).
[61]S. F. Gimelshein, "Particle modeling of reflected shock waves," J. Thermophys. Heat Transfer **35**, 1–10 (2020).
[62]J. G. Kim and I. D. Boyd, "Thermochemical nonequilibrium analysis of O_2+Ar based on state-resolved kinetics," Chem. Phys. **446**, 76–85 (2015).